

## TOPICAL REVIEW

# The science and technology of superconducting cavities for accelerators

Hasan Padamsee

Cornell University, Ithaca, NY 14853, USA

Received 15 August 2000, in final form 16 January 2001

### Abstract

Rapid advances in the performance of superconducting cavities have made RF superconductivity a key technology for accelerators that fulfil a variety of physics needs: high-energy particle physics, nuclear physics, neutron spallation sources and free-electron lasers. New applications are forthcoming for frontier high-energy physics accelerators, radioactive beams for nuclear astrophysics, next-generation light sources, intense proton accelerators for neutron and muon sources. There are now nearly one kilometre of superconducting cavities installed in accelerators around the world, providing more than 5 GV of acceleration. The most recent installation of 20 m for a free-electron laser realized an average gradient a factor of four higher than existing applications. Improved understanding of the physics of RF superconductivity, together with advances in technology, are responsible for the spectacular increases in performance. RF superconductivity is a mature science going well beyond technological know-how and trial-and-error approaches to genuine understanding of the underlying physics. Research continues to push performance levels towards the theoretical limit, which is another factor of two higher than the levels yet achieved.

## 1. The benefits of RF superconductivity

Superconducting RF (SRF) cavities excel in applications requiring continuous wave (CW) or long-pulse accelerating fields above a few million volts per metre ( $\text{MV m}^{-1}$ ). We often refer to the accelerating field as the ‘gradient’. Since the ohmic power loss in the walls of a cavity increases as the square of the accelerating voltage, copper cavities become uneconomical when the demand for high CW voltage grows with particle energy. A similar situation prevails in applications that demand a long RF pulse length, or a high RF duty factor. Here superconductivity brings immense benefits. The surface resistance of a superconducting cavity is many orders of magnitude less than that of copper. After accounting for the refrigerator power needed to provide the liquid helium operating temperature, a net gain factor of several hundred remains to provide many advantages.

Copper cavities are limited to gradients well below a few megavolts per metre in CW and long-pulse operation because the capital cost of the RF power and the ac-power operating cost becomes prohibitive. For example, several megawatts per metre of RF power are required to operate a copper cavity at

$5 \text{ MV m}^{-1}$ . There are also practical limits to dissipating high power in the walls of a copper cavity. The surface temperature becomes excessive, causing vacuum degradation, stresses and metal fatigue due to thermal expansion.

On the other hand, copper cavities offer higher accelerating fields ( $\approx 100 \text{ MV m}^{-1}$ ) for short pulse (microsecond) and low duty factor ( $< 0.1\%$ ) applications. Still, for such applications it is important to provide abundant peak RF power (e.g.  $100 \text{ MW m}^{-1}$ ) and to withstand the aftermath of intense voltage breakdown in order to reach the high fields.

There is another important advantage that SRF cavities bring to accelerators. The presence of accelerating structures has a disruptive effect on the beam, limiting the quality of the beam in aspects such as energy spread, beam halo or even the maximum current. Because of their capability to provide higher voltage, SRF systems can be shorter, and thereby impose less disruption. Due to their high ohmic losses, the geometry of copper cavities must be optimized to provide a high electric field on-axis for a given wall dissipation. This requirement tends to push the beam aperture to small values, which disrupts beam quality. By virtue of low wall losses, it is affordable to design an SRF cavity to have a large beam hole,

reduce beam disruption and provide high quality beams for physics research.

The plan of this article is to present a brief review of the applications to be followed by a discussion of the basics of accelerating structures and RF superconductivity. Next we discuss issues governing the choice of cavity shape, materials and fabrication techniques suitable for the different materials. The major topics in RF superconductivity are the nature of RF surface resistance and the phenomena that occur at high RF fields.

## 2. A brief review of applications

Many review articles [1–6] are now available covering the state of the art in RF superconductivity and its application to particle accelerators. There have been nine international workshops on RF superconductivity. A reference text [7] is available. The discussion here is an overall summary and review with emphasis on the science and technology of the materials and new developments. We refer the reader to the reference text for a more thorough discussion of many of the standard topics in RF superconductivity.

There are now nearly one kilometre of superconducting cavities installed in electron accelerators around the world providing more than 5 GV of acceleration. The two largest installations are CEBAF at the Jefferson Laboratory in the USA [8], and LEP-II at CERN in Europe [9]. CEBAF provides electron beams of energy up to 5 GeV for nuclear physics. LEP-II collides electron and positron beams, each with 100 GeV energy for high-energy particle physics. Over the period of a few years CEBAF has upgraded the in-line accelerating gradient of their sheet metal niobium cavities from the design value of 5 to 7 MV m<sup>-1</sup>. With equal success, LEP-II upgraded the in-line performance of their niobium-on-copper (Nb/Cu) cavities from 6 to 7 MV m<sup>-1</sup>, reaching the highest energy electron–positron collisions: 200 GeV in the *centre of mass*. The performance upgrades at CEBAF and LEP realized the intrinsic, high-gradient potential of SRF cavities.

In high-current applications which are intended for high-energy physics at the highest possible luminosity, superconducting cavities support beam currents of more than 600 mA as compared to CEBAF and LEP beam currents of less than 10 mA. The main systems here are: CESR (Cornell Electron Storage Ring) in the USA [10], and the KEK B-factory in Japan [11], both operating for copious production of mesons comprised of the B-quarks. The operating gradients at CESR and KEK-B are also 7 MV m<sup>-1</sup>.

New applications of SRF are forthcoming for high-energy and high-luminosity electron–positron colliders, proton–proton colliders, storage ring light sources, free-electron lasers, intense proton linacs for neutron and muon sources, muon recirculating linacs for neutrino sources in the near future and high-energy muon colliders in the far future. Some of the new applications demand high beam currents, and therefore high beam power. Other applications demand the highest possible gradients. Some require CW operation, others demand pulse lengths in the millisecond range. The important challenge for all future applications is to achieve high gradients ( $E_{acc}$ ) reliably at low wall dissipation, i.e. with high  $Q_0$ . Here  $Q_0$  is the quality factor for a resonator, to be discussed in section 3.2.

The largest of these applications is likely to be for TESLA, a TeV Energy Superconducting Linear Accelerator [12]. To achieve beam energy in the TeV class will require 33 km of superconducting cavities operating at gradients of 30 MV m<sup>-1</sup>. To address the developments needed for such a mammoth facility, there is an international collaboration centred at DESY (Hamburg, Germany) where a test facility is underway, called the TTF (for TESLA Test Facility) [12].

In anticipation of the needs for TESLA, the achievable gradient of sheet metal niobium cavities has more than doubled since the large installations at CEBAF and LEP. Figure 1 shows the impact of technology breakthroughs by comparing Year 1995 CEBAF performance with Year 2000 TTF performance. For both cases we give the performance of the bare cavities as measured in a vertical test dewar. Such measurements provide an excellent gauge for the intrinsic potential of cavities.

## 3. Basics of accelerating structures

The accelerating device is an electromagnetic cavity resonating at a microwave frequency between 50 and 3000 MHz. There are two distinct types of cavities, depending on the velocity of the particles. The first category is for accelerating charged particles that move at nearly the speed of light, such as electrons in a high-energy linear accelerator or in an electron storage ring. Our review focuses on this type of cavity, see figure 2. The second type of cavity is for particles that move at a small fraction (e.g. 0.01–0.3) of the speed of light [13], such as the heavy ions emerging from a dc high-voltage Van de Graaff accelerator, or from an electron cyclotron resonance source. The design and experience of low-velocity resonators is sufficiently different to deserve a separate review, although many of the materials issues are common.

### 3.1. Key properties for the performance accelerating cavities

For real structures with contoured shapes, beam apertures and beam pipes, it is necessary to use field computation codes, such as MAFIA [14]. Only simple structures can be calculated analytically, such as a cylinder with no beam holes (figure 3), referred to as the ‘pill-box cavity’. For our purposes, the analytic calculations of a simple cylindrical cavity are convenient to define the important performance parameters of superconducting cavities. For a cylinder of length  $d$  and radius  $R$  using cylindrical coordinates  $(\rho, \phi, z)$ , the electric ( $E_z$ ) and magnetic ( $H_\phi$ ) fields for the TM<sub>010</sub> mode are given by

$$E_z = E_0 J_0 \left( \frac{2.405\rho}{R} \right) e^{-i\omega t}$$

and

$$H_\phi = -i \sqrt{\frac{\epsilon_0}{\mu_0}} E_0 J_1 \left( \frac{2.405\rho}{R} \right) e^{-i\omega t}$$

where all other field components are zero.  $J_0$  and  $J_1$  are Bessel functions. The angular resonant frequency is given by

$$\omega_{010} = \frac{2.405c}{R}$$

which is independent of the cavity length.

First we determine the accelerating field,  $E_{acc}$ . Assume an electron travelling nearly at the speed of light ( $c$ ). It enters

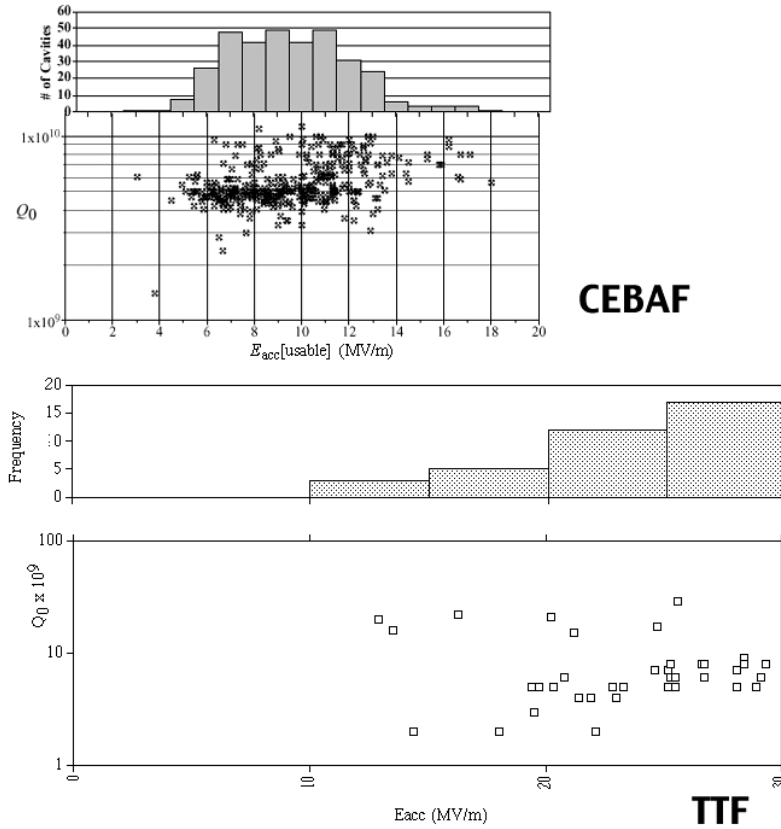


**Figure 1.** A comparison between CEBAF and TTF gradients and  $Q_0$  values for the vertical test results.  $Q_0$  is the quality factor of a resonator, discussed in section 3.2. The histograms show the distribution of the maximum gradients reached with the available RF power. The accompanying scatter plot gives the  $Q_0$  at the maximum gradient. The upper panels—labelled CEBAF—show the gradient and  $Q$  statistics of more than 300 five-cell, 1.5 GHz Cornell on CEBAF cavities. The lower panels—labelled TTF—give the recent statistics in the performance of about 40 nine-cell, 1.3 GHz cavities tested at the TTF. Although at this stage the number of TTF cavities is less than 60, note that the nine-cell cavities have more than twice the surface area of the five-cell, CEBAF cavities. As we will see, a larger surface area is a greater challenge for achieving high gradients.

the cavity at time  $t = 0$  and leaves at a time  $t = d/c$ . To receive the maximum kick from the cavity, the time it takes the particle to traverse the cavity is to equal half an RF period (TRF), i.e.

$$t = \frac{d}{c} = \frac{1}{2} T_{RF} = \frac{\pi}{\omega}.$$

In this case, the electron always sees a field pointing in the same direction. The accelerating voltage ( $V_{acc}$ ) for a cavity is

$$V_{acc} = \left| \int_{z=0}^{z=d} E_{el} dz \right|.$$

For an electron accelerator with energy greater than 10 MeV, it is sufficiently accurate to use  $v = c$ , so that  $t(z) = z/c$ . Thus

$$V_{acc} = \left| \int_{z=0}^{z=d} E_z(\rho = 0, z) e^{i\omega z/c} dz \right|$$

$$V_{acc} = E_0 \left| \int_{z=0}^{z=d} e^{i\omega z/c} dz \right| = d E_0 \frac{\sin(\omega d/(2c))}{\omega d/(2c)} = d E_0 T.$$

At a 1.5 GHz RF frequency,  $d = c/\lambda = 10$  cm and  $V_{acc}$  simplifies to

$$V_{acc} = (2/\pi) d E_0.$$

The average accelerating electric field ( $E_{acc}$ ) that the electron sees during transit is given by

$$E_{acc} = \frac{V_{acc}}{d} = \frac{2E_0}{\pi}.$$

### 3.2. Peak surface fields

To maximize the accelerating field it is important to minimize the ratios of the peak fields to the accelerating field by selecting a suitable cavity geometry. For the  $TM_{010}$  accelerating mode in a pill-box cavity

$$E_{pk} = E_0$$

and

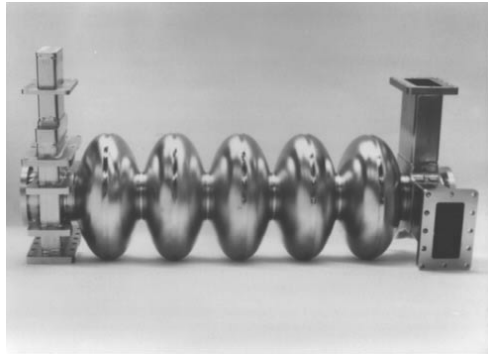
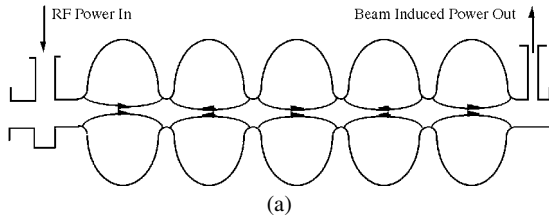
$$H_{pk} = \sqrt{\frac{\epsilon_0}{\mu_0}} J_1(1.841) E_0 = \frac{E_0}{647 \Omega}.$$

Thus we obtain the following ratios:

$$\frac{E_{pk}}{E_{acc}} = \frac{\pi}{2} = 1.6$$

and

$$\frac{H_{pk}}{E_{acc}} = 2430 \frac{\text{A m}^{-1}}{\text{MV m}^{-1}} = 30.5 \frac{\text{Oe}}{\text{MV m}^{-1}}.$$



(b)

**Figure 2.** (a) An accelerating structure for light particles. The resonant frequency is typically between 350 and 3000 MHz. The cell length is half a wavelength ( $\lambda/2$ ) long. There are five accelerating cells that resonate in the  $TM_{010}$  mode of the cylindrical cavity. As the particle traverses each accelerating gap in half an RF period, it sees the electric field pointing in the same direction, so that there is continuous acceleration. The phase of the electric field on the axis of each cell is shown for the accelerating mode. Ports outside the cell region are for input couplers that provide power for the field and the beam. Other ports are for output couplers that extract power deposited by the beam in higher-order modes. (b) A five-cell, 1.5 GHz niobium cavity—Cornell/CEBAF cavity. The active length is 0.5 m.

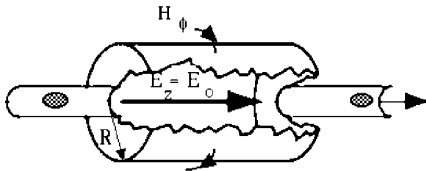


**Figure 3.** A pillbox cavity showing electric and magnetic fields.

The peak field ratios for a realistic structure are much larger. For example, for the TTF cavity,  $E_{pk}/E_{acc} = 2.0$  and  $H_{pk}/E_{acc} = 42 \text{ Oe} (\text{MV m}^{-1})$ .

### 3.3. Power dissipation and $Q$

In order to support the fields in the cavity, currents flow within a thin surface layer of the cavity walls. If the surface resistance is  $R_s$ , the power dissipated per unit area ( $P_a$ ) due to Joule heating is

$$P_a = \frac{1}{2} R_s H^2.$$

The two most salient characteristics of an accelerating cavity are its average accelerating field,  $E_{acc}$ , and the intrinsic quality factor  $Q_0$ . We have just discussed  $E_{acc}$ . The quality ( $Q_0$ ) is related to the power dissipation by the definition of  $Q_0$

$$Q = \omega \frac{\text{Energy stored}}{\text{Power dissipated}} = \frac{\omega U}{P_c}$$

where  $U$  is the stored energy and  $P_c$  is the dissipated power.

Since the energy stored in the electric field is equal to that stored in the magnetic field, the total energy in the cavity is given by the power dissipated as

$$U = \frac{1}{2} \mu_0 \int_v |H|^2 dv \quad P_c = \frac{1}{2} R_s \oint_s |H|^2 ds$$

where the first integral is taken over the volume of the cavity and the second over the surface. Thus

$$Q = \frac{\omega \mu_0 \int_v |H|^2 dv}{R_s \oint_s |H|^2 ds}$$

$$Q = \frac{G}{R_s} \quad G = \frac{\omega \mu_0 \int_v |H|^2 dV}{\oint_s |H|^2 ds}.$$

Here  $G$  is called the ‘geometry factor’ for the cavity shape. For a pill box in the  $TM_{010}$  mode,  $G = 257 \Omega$ . A typical observed surface resistance for a well prepared superconducting Nb cavity is  $R_s = 20 \text{ n}\Omega$ . Thus we have a  $Q_0$  value of

$$Q = \frac{G}{R_s} = 1.3 \times 10^{10}.$$

For a typical cavity length of  $d = 10 \text{ cm}$  and a RF frequency of 1.5 GHz, the cavity radius is  $R = 7.65 \text{ cm}$ . For an accelerating voltage of 1 MV, the following values for the important features of a superconducting accelerating cavity are obtained:

$$E_{acc} = \frac{V_{acc}}{d} = 10 \text{ MV m}^{-1}$$

$$E_{pk} = E_0 = \frac{\pi}{2} E_{acc} = 15.7 \text{ MV m}^{-1}$$

$$H_{pk} = 2430 \frac{\text{A m}^{-1}}{\text{MV m}^{-1}} \quad E_{acc} = 24.3 \text{ kA m}^{-1} = 305 \text{ Oe}$$

$$U = \frac{\pi \epsilon_0 E_0^2}{2} J_1^2(2.405) d R^2 = 0.54 \text{ J}$$

$$P_c = \frac{\omega U}{Q} = 0.4 \text{ W}.$$

## 4. Basics of RF superconductivity

As explained in the general reference text [7], the remarkable properties of superconductivity are attributed to the condensation of charge carriers into Cooper pairs, which then move without friction; hence the zero resistance. At  $T = 0 \text{ K}$ , all charge carriers condense. At higher temperatures, pairs break up. The fraction of unpaired carriers increases exponentially with temperature, as  $e^{-\Delta/kT}$ , until none of the carriers are paired above  $T_c$ —the normal conducting state. Here  $2\Delta$  is the energy gap of the superconductor, i.e. the energy needed to break up the pairs. In this simplified picture, known as the London two-fluid model, when a dc field is turned on, the pairs carry all the current, shielding the applied field from the normal electrons. Electrical resistance vanishes since Cooper pairs move without friction.

In the case of RF currents, however, dissipation does occur for all  $T > 0 \text{ K}$ , albeit very small compared to the normal conducting state. While the Cooper pairs move without friction, they do have inertial mass. For high-frequency currents to flow forces must be applied to bring about

alternating directions of flow. Hence an ac electric field will be present in the skin layer, and it will continually accelerate and decelerate the normal carriers, leading to dissipation proportional to the square of the RF frequency. A simplified form of the temperature dependence of Nb for  $T_c/T > 2$  and for frequencies much smaller than  $2\Delta/h \approx 10^{12}$  Hz is

$$R_S = A(1/T)f^2 \exp(-\Delta(T)/kT) + R_0.$$

Here  $A$  is a constant that depends on material parameters, as we will discuss in section 6. The operating temperature of a superconducting cavity is usually chosen so that the temperature-dependent part of the surface resistance is reduced to an economically tolerable value.  $R_0$ , referred to as the residual resistance, is influenced by several factors to be discussed in section 7.

The accelerating field,  $E_{acc}$ , is proportional to the peak electric ( $E_{pk}$ ) as well as the magnetic field ( $H_{pk}$ ) on the surface of the cavity—as discussed in section 3. Therefore the other important fundamental aspects of superconducting cavities are the maximum surface fields that can be tolerated without substantially increasing the microwave surface resistance, or without causing a catastrophic breakdown of superconductivity. The ultimate limit to the accelerating field is the RF critical magnetic field, above which the superconducting phase can no longer exist. The RF critical field is related to the thermodynamic critical field. In the process of a phase transition to the normal conducting state, a phase boundary must be nucleated. Because of the rapidly changing RF fields (nanosecond time scale), it is possible for the Meissner state to persist above the thermodynamic critical field ( $H_c$ ) for type I superconductors, and above the lower critical field ( $H_{c1}$ ) for type II superconductors. Such a metastable situation can be expected up to a superheating critical field,  $H_{sh} > H_c$  (type I)  $> H_{c1}$  (for type II). It is important to note that the RF critical field does *not* depend on  $H_{c2}$ . Therefore high-field magnetic materials, such as Nb–Ti, do not offer correspondingly higher operating fields for superconducting cavities. Indeed for RF superconductivity, it is essential to always operate in the Meissner state. It is even possible that the precipitates which serve as excellent pinning centres for the dc flux lines may be harmful to the performance of SRF cavities. For the most popular superconductor, niobium,  $H_{sh}$  is about 0.23 T, and for Nb<sub>3</sub>Sn it is 0.4 T. These surface fields translate to a maximum accelerating field of 55 MV m<sup>-1</sup> for a typical niobium structure and 95 MV m<sup>-1</sup> for a Nb<sub>3</sub>Sn cavity. The exact values depend on the detailed structure geometry.

Typical cavity performance is significantly below the theoretically expected surface field limit. One important phenomenon that limits the achievable RF magnetic field is the ‘thermal breakdown’ of superconductivity, originating at submillimetre-size regions of high RF loss, called defects. When the temperature outside the defect exceeds the superconducting transition temperature,  $T_c$ , the losses increase substantially, as large regions become normal conducting. Thermal breakdown is the subject of extensive discussion, in section 8. Here we also discuss measures available to overcome thermal breakdown such as (a) improving the thermal conductivity of niobium by purification and (b) using thin films of niobium on a copper substrate cavity.

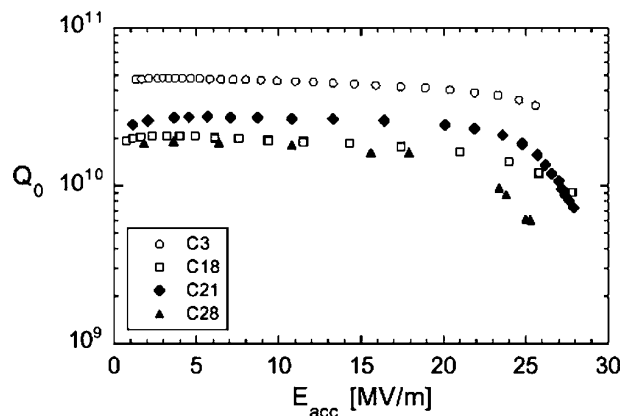


**Figure 4.**  $Q_0$  against  $E$  curves for nine-cell, 1.3 GHz cavities. When x-rays are also present, the  $Q$  drop is attributed to field emission [16].

In contrast to the magnetic field limit, we know of no theoretical limit to the tolerable surface electric field. Fields up to 220 MV m<sup>-1</sup> have been imposed on a superconducting niobium cavity without any catastrophic effects [15]. However, at high electric fields an important limitation to the performance of superconducting cavities arises from the emission of electrons from local spots in the high electric field regions of the cavity. This is a problem endemic to all high-voltage devices. Power is absorbed by the electrons and deposited as heat upon impact with the cavity walls. Copious x-rays are emitted due to bremsstrahlung. When the emission grows intense at high electric fields it can even initiate thermal breakdown. In many cases intense field emission eventually leads to momentary voltage breakdown of the vacuum in the cavity. This has mostly a beneficial effect for superconducting cavities, known as conditioning. After a voltage breakdown event, it is usually possible to raise the electric field until field emission grows intense once again at another spot on the cavity surface. We have learned much about the nature of field emission sites and made progress in techniques to avoid them as well as to destroy them by conditioning with high-voltage breakdowns (section 10).

In the early stages of the development of superconducting cavities, a major performance limitation was ‘multipacting’. This is a resonant process in which an electron avalanche builds up within a small region of the cavity surface due to a confluence of several circumstances. With the invention of the proper cavity shape, multipacting is no longer a significant problem for velocity-of-light structures. The essential idea to avoid multipacting is to gradually curve the outer wall of the cavity—hence the curved profile.

The history of advances in superconducting cavities shows that as the limiting mechanisms of multipacting, thermal breakdown and field emission were each understood, and in turn overcome, cavity performance has improved steadily over time. Today, single-cell cavities exceed accelerating fields of 40 MV m<sup>-1</sup>, not far from the theoretical limit imposed by the RF critical field. Full-scale structures, ready for beam, reach gradients of 25 MV m<sup>-1</sup>. Whether the Nb critical magnetic field limit can be surpassed by using a different material—such as Nb<sub>3</sub>Sn—remains an open and interesting issue.

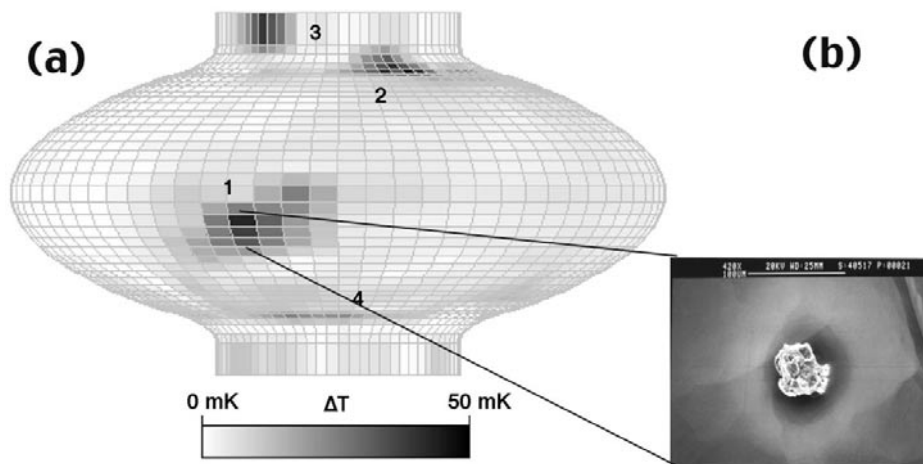


**Figure 5.** (a) Temperature map at 400 Oe of a 1.5 GHz, single-cell cavity showing heating at a defect site, labelled 1, and field emission sites labelled 2, 3, and 4. (b) SEM micrograph of the RF surface taken at site 1 [17].

The performance of a superconducting cavity is evaluated by measuring the  $Q_0$  as a function of the cavity field level. These curves bear tell-tale signs of the activities inside the cavity. Figure 4 shows  $Q_0$  against  $E$  curves for some of the best performing multi-cell structures [16]. These are the nine-cell cavities for the TTF. Here the exponential drop in  $Q_0$  with field suggests that field emission is the dominant limiting mechanism, provided x-rays are also observed. But the  $Q_0$  against  $E_{acc}$  curve only gives information on the average behaviour of the RF surface. To resolve the local distribution of RF losses and identify various mechanisms, temperature mapping proves to be a powerful diagnostic technique. A chain of rotating carbon thermometers, or an array of fixed thermometers, samples the temperature of the outer wall of the cavity. A typical temperature map is shown in figure 5 [17]. Once the hot spot is located, the RF surface can be examined by a surface analytic instrument. In the case of figure 5, an SEM examination revealed a copper particle the base of which was partially melted and bonded to the Nb surface. Such a spot constitutes a normal conducting defect with the potential to cause the thermal breakdown of superconductivity.

## 5. Choice of cavity shape and fabrication technologies

There are many factors which influence the cavity shape. Beam dynamics considerations control the size of the aperture. To lower the peak electric field it is necessary to round the iris region with circular or elliptical arcs. Peak magnetic field considerations influence the shape of the cavity in the large diameter (equator) region where the magnetic field is strongest. Elliptical arc segments increase the strength of the cavity against atmospheric load and also provide a slope for efficient rinsing of liquids during surface etching and cleaning.

Multipacting is a key factor that governs the overall rounded contour of the cavity profile [18]. If the shape is not rounded, one-surface multipacting will severely limit the cavity performance (figure 6). An electron emitted from one region of the surface (usually the outer cylindrical wall) travels in a cyclotron orbit in the RF magnetic field, and returns to

near its point of origin. Upon impact it generates a secondary electron which mimics the trajectory of the primary. An exponential build up occurs if the round-trip travel time of each electron is an integer multiple of an RF period, i.e. the electron returns in the same phase of the RF period as it was generated. For the build up to persist, the secondary emission coefficient must be greater than one. This is true for a niobium surface when the electron energy is between 50 and 1000 eV (see [7]). During their excursion into the RF fields, the electrons must gain enough energy from the electric field to generate secondaries on impact. When these conditions are met, an electron avalanche occurs, absorbing the RF power and making it impossible to raise the fields by increasing the incident RF power. The electrons impact the cavity walls, which leads to a large temperature rise, thermal breakdown, and in some cases a momentary gas discharge. When the cell shape is rounded (figure 6) the electrons are forced to the equator region where the electric field is too low for the electrons to gain sufficient energy to regenerate. The avalanche is arrested.

For a material to be useful for accelerators, the primary requirements are a high transition temperature,  $T_c$ , and a high RF critical magnetic field,  $H_{sh}$ . Among the elemental superconductors, niobium has the highest  $T_c$  and the highest RF critical field. Accordingly, it is a most attractive choice for accelerator cavities. Successful cavities have been made from sheet Nb, or by sputtering Nb onto a copper cavity. The realm of superconducting compounds has been much less explored because of technical complexities that govern compound formation. In looking at compound candidates, it is important to select a material for which the desired compound phase is stable over a broad composition range so that formation of the compound is more tolerant to variations in experimental conditions, making it possible to achieve the desired single phase over a large surface area.  $Nb_3Sn$  is a promising material; its  $T_c$  is 18 K and the RF critical field is 0.4 T, twice as high as for Nb. On fundamental grounds the higher field opens up the possibility of accelerating gradients higher than allowed for niobium cavities. However, the performance for  $Nb_3Sn$  cavities to date is far lower than for niobium cavities. For reasons we will discuss, the new

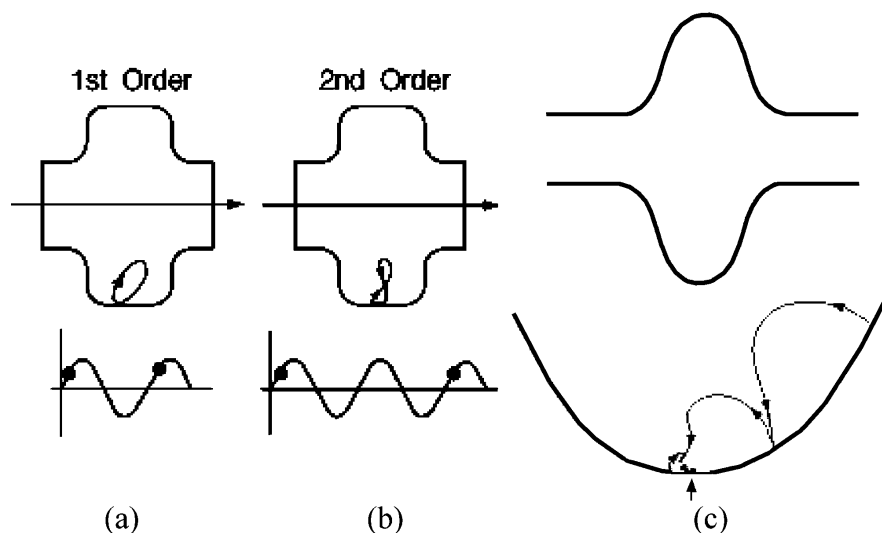


**Figure 6.** (a) In a cavity with a nearly pill-box-like shape, electrons can multiply in the region shown. The electron returns in an integer multiple of RF period. The number of RF periods is called the order of multipacting. (b) The favourable (for multipacting) start and end phases of the electron that returns in two RF periods. A travel time of one RF period results in first-order multipacting. (c) When the cavity shape is rounded, the electrons drift to the zero-field region at the equator. Here the electric field is so low that the secondary cannot gain enough energy to regenerate.

high-temperature superconductors (HTS) are even further from the microwave performance level desired for application to accelerators.

### 5.1. Sheet niobium

Technical considerations, such as ease of fabrication and the ability to achieve uniformly good material properties over a large surface area, are very favourable for fabricating cavities from niobium sheet. The typical sheet thickness selected is a few millimetres. High-purity sheet niobium is readily available, has a reasonably high thermal conductivity, is mechanically workable to form cavity shapes and can be electron beam welded without introducing excess RF losses at joints. The purity of niobium used is important, both in terms of bulk purity, as well as inclusions from manufacturing steps, such as rolling. Inclusions on the RF surface play the role of normal conducting sites for thermal breakdown of superconductivity. Therefore the niobium material must be prepared with great care to keep it free from defects. In a new development at the DESY TTF, the starting niobium sheet is scanned for defects by eddy-current scanning [19]. Figure 7 shows a typical defective sheet found by deploying a rotating, eddy-current scanning instrument. For the TTF project, less than 5% of more than 200 sheets scanned showed defects that warranted rejection of the starting sheet.

Another class of harmful impurities is dissolved interstitial oxygen, carbon, nitrogen and hydrogen, which serve as scattering sites for the electrons not condensed into Cooper pairs. These impurities lower the thermal conductivity and limit the maximum tolerable surface magnetic field before the onset of thermal breakdown. The accompanying increase in electrical conductivity, or the  $RRR$  value, serves as a convenient measure of the purity of the metal. The formal definition of  $RRR$  is

$$RRR = \frac{\text{resistivity at 300 K}}{\text{residual resistivity at low temperature (normal state)}}$$

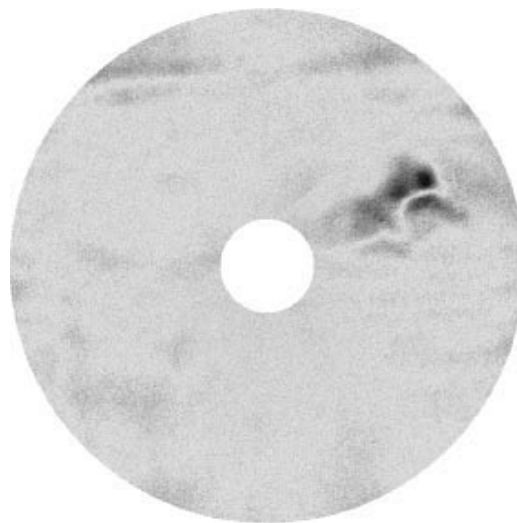


**Figure 7.** Material defect found with eddy-current scanning on a rotating turntable. The sheet diameter is about 25 cm.

Figure 8 shows the thermal conductivity of Nb parametrized with increasing  $RRR$  [20]. Niobium is now available with  $RRR = 250$ –400 from US, European and Japanese suppliers who use the techniques of multiple and slow electron beam melting. As industries continue to improve their vacuum practices, the  $RRR$  continues to rise. Although  $RRR = 400$  is the highest available from industry, a cavity can be post-purified after fabrication to achieve purity levels corresponding to  $RRR = 600$ –1000. Higher  $RRR$  provides the best insurance against thermal breakdown, especially when the construction of an accelerator calls for a large batch of cavities, each with surface areas of the order of a square metre.

The most common fabrication method of cavities from sheet is to deep draw or spin half-cells (figure 9). Sheet metal forming is sensitive to mechanical properties. In particular, a

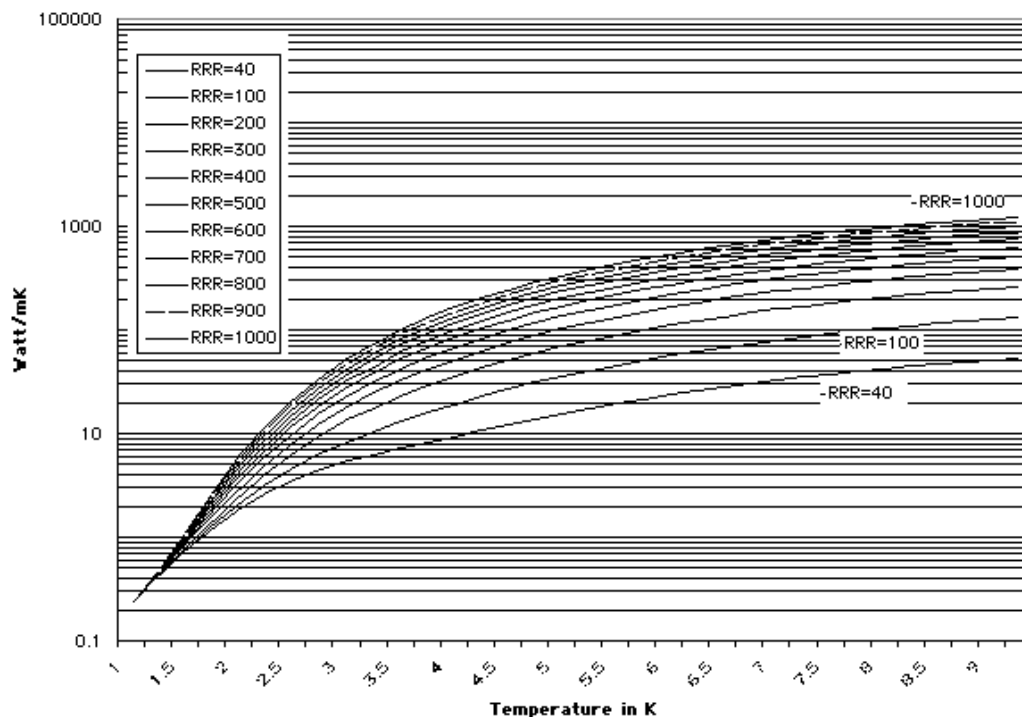


Figure 8. Calculated thermal conductivity of Nb as *RRR* (and purity) increase.

small and uniform grain size ( $<50 \mu\text{m}$ ) is essential, as shown in figure 10. After forming and trim machining, the parts are electron beam welded together under a vacuum better than  $10^{-5}$  Torr. The weld parameters must be chosen to give a smooth bead by using a defocused or rastered beam. In recent developments, techniques are being developed to fabricate weld-free cavities by spinning from a single sheet or a tube [21], as well as hydroforming from a tube [22]. Seamless multi-cell cavities by spinning [21] from a single sheet of copper have also been made (figure 11), and will provide substantial cost savings for future large projects.

To achieve the best RF performance, the surface of the cavity must be as close as possible to the ideal. Chemical etching or electropolishing to a depth of  $100\text{--}200 \mu\text{m}$  removes mechanically damaged layers. Figure 12 compares optical micro-graphs of chemical etched and electropolished surfaces [23]. Obviously the electropolished surface is much smoother. Recently, this has been shown to be important for reaching accelerating fields above  $20 \text{ MV m}^{-1}$ . After etching, the cavity is thoroughly rinsed in  $18 \text{ M}\Omega \text{ cm}$  purity, dust-free water. From here on, the surface must be exposed only to dust-free, clean air, semiconductor-grade, Class 100 or better. This means that the air must be filtered to have fewer than 100 particles larger than  $1 \mu\text{m}$  in size in a volume of 100 cu.ft.

## 5.2. Nb/Cu

A strong motivation for using thin films of Nb on copper cavities is to provide increased stability against thermal breakdown of superconductivity. The thermal conductivity of copper at 4.2 K is between  $300$  and  $2000 \text{ W m}^{-1} \text{ K}^{-1}$ , depending on the purity and annealing conditions, as compared to the thermal conductivity of  $300 \text{ RRR}$  of niobium, which is  $75 \text{ W m}^{-1} \text{ K}^{-1}$  at 4.2 K (figure 8). The cost saving of niobium

material is another potential advantage, significant for large-size, for example 350 MHz cavities such as for LEP-II, or for future projects which aspire to make 200 MHz cavities, where each cell is nearly 1.5 m in diameter.

After an extensive programme to determine the best copper cleaning and niobium coating methods at CERN and at industrial vendors, nearly 300 four-cell cavities have been successfully produced at LEP [24]. The base copper cavity is made by the same methods as the sheet metal niobium cavities, i.e. forming half-cells by spinning, trim machining, cleaning, electropolishing, and electron beam welding.

In the most successful coating method to date [25], thin-film deposition is carried out by cylindrical magnetron sputtering (figure 13). Before the coating stage, the copper cavity is degreased, electrolytically etched, rinsed with high-purity, dust-free water and alcohol and dried under a clean laminar air-flow. Chemical etching of the copper substrate produces pin holes and should be avoided. After a bakeout of the copper cavity at  $150^\circ\text{C}$  for 24 h to reach a good vacuum, the cavity is coated with a Nb film by magnetron sputtering. A typical coating time is 4 h at a discharge pressure of  $1.5 \times 10^{-3}$  mbar. The coating thickness is a few micrometres at a substrate temperature of  $180\text{--}200^\circ\text{C}$ .

The *RRR* of the deposited niobium serves as one of the monitors of film quality. The sputtering rate and substrate temperature should be optimized to reach a *RRR* greater than 10 for the Nb film. Note that the low *RRR* relative to bulk niobium is not a problem because the film is only micrometres thick. Extensive studies have been carried out with various sputtering gases, such as Ar, Kr, Xe and Ne [26].

The rod-like grains of the niobium film are up to  $1 \mu\text{m}$  long and  $10\text{--}150 \text{ nm}$  in diameter (figure 14). For films grown on an oxide-free copper surface, the grain size is in the

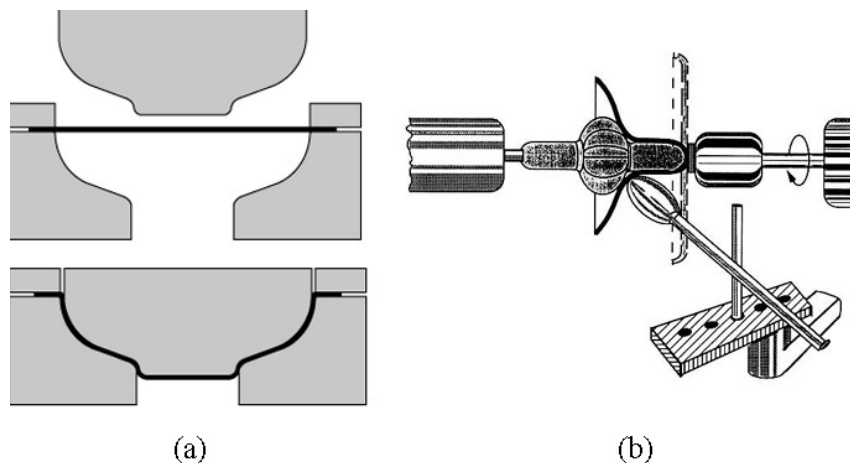


**Figure 9.** Schematic diagrams for (a) deep drawing and (b) spinning.

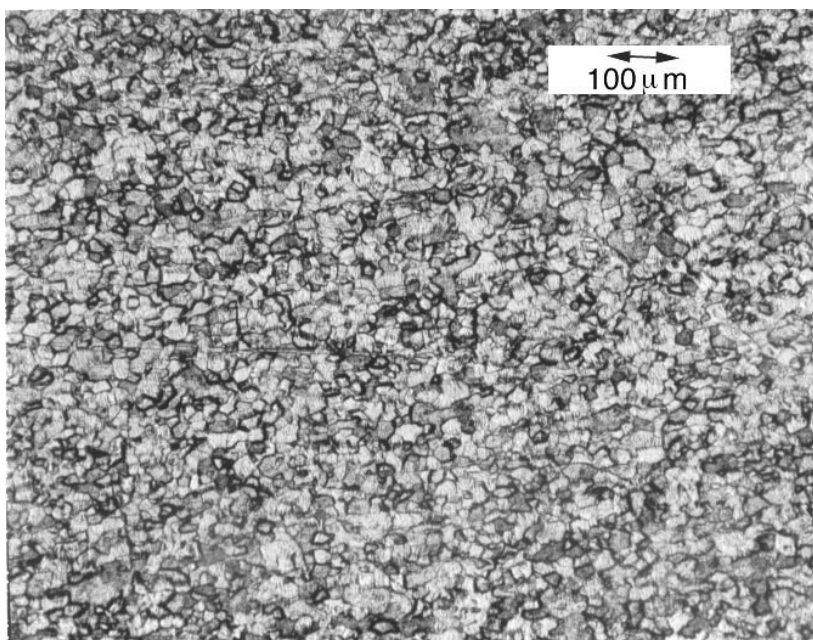


**Figure 10.** Optical micrograph showing the small and uniform grain size essential for good forming properties. Here the grain size is about  $50\ \mu\text{m}$ .

micrometre range. When studied with electron microscopy, the individual grains show a high density of defects, consisting of dislocations and point defect agglomerates [27]. The distance between two defects varies from 2 to 20 nm. The onset  $T_c$  of the films when removed from the copper substrate is 9.2 K, but the transition width is larger than for bulk niobium, stretching to 5 K in some cases. While on the substrate, the  $T_c$  of the films is higher, for example 9.6 K, due to the compressive stress arising from the mismatch in the expansion coefficients of niobium and copper.

### 5.3. $\text{Nb}_3\text{Sn}$

The main fabrication technique pursued for cavities has been through vapour diffusion of tin into niobium, at a reaction temperature of  $1200^\circ\text{C}$ . The solid-state reaction procedure is outlined in figure 15 [28]. The tin source sits in a tungsten crucible underneath the niobium cavity and inside a long

niobium tube. The temperature of the tin source, and therefore the tin vapour pressure, is controlled independently of the temperature of the cavity. This feature allows good nucleation of the correct phase, and prevents excess tin at the surface. The purity ( $RRR$ ) of the niobium cavity is protected by using titanium on the outside of the cavity, as discussed in section 8.

In the bakeout part of the heating cycle, the cavity and source are heated to  $200^\circ\text{C}$  for outgassing, after which the cavity is closed *in situ* with a niobium lid, making a sealed reaction chamber. In the first stage of compound formation, both source and cavity are heated for 5 h to  $500^\circ\text{C}$  for the nucleation of the  $\text{Nb}_3\text{Sn}$  layer, which is promoted by the addition of  $\text{SnCl}_2$  in the source crucible. In the reaction stage, the source is held at  $1100^\circ\text{C}$ , and the cavity at  $1200^\circ\text{C}$  for 3 h. The tin vapour pressure is estimated to be  $10^{-3}$  mbar. Finally, the source heater is switched off 30 min before the

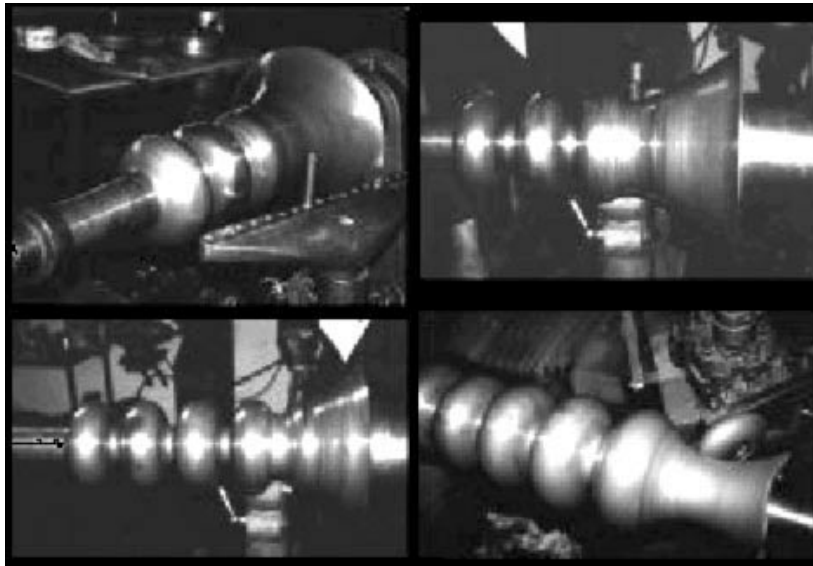


**Figure 11.** Spinning a multicell cavity from a single sheet [21].

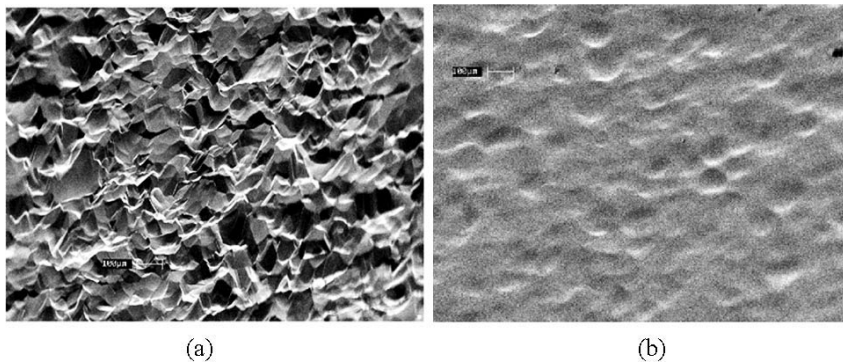


**Figure 12.** Comparison of optical micrographs of a niobium surface prepared by (a) standard chemical polishing and (b) electropolishing. Typical grain size is  $50 \mu\text{m}$  [23].

cavity heater so as to avoid excess tin deposition at the RF surface. The thickness of the resulting compound layer is about  $2 \mu\text{m}$ , and the average grain size is also about  $2 \mu\text{m}$  as shown in the micrograph of figure 15. By independently controlling the temperature of the tin source during the reaction, it is possible to both obtain good nucleation and avoid excess tin.

#### 5.4. HTS materials

Since the high  $T_c$  revolution, more than 100 superconducting compounds have been found with a  $T_c$  above 23 K. The most commonly studied material is YBCO with a  $T_c$  of about 90 K. Epitaxial films with the best RF properties have been prepared by laser ablation, electron beam coevaporation and sputtering. For respectable RF properties, the films are grown so that  $c$ -axis of the YBCO crystal plane is normal to the RF surface everywhere. This restriction will prove to be a serious challenge for realizing HTSs in existing cavity shapes. Besides proper orientation, the fabrication of good material poses many difficulties. It is essential to obtain the right stoichiometry and oxygen content over large areas. Because of the short coherence

length of HTS materials, the RF properties are extremely sensitive to minute defects, such as grain boundaries and their associated imperfections. Decoupling of superconducting grains is believed to occur, and only weak links can exist between grains, which leads to intergranular losses [29].

## 6. Surface resistance

Based on the very successful Bardeen–Cooper–Schrieffer (BCS) theory, expressions for the superconducting surface impedance have been worked out by Mattis and Bardeen [30] and by others. These expressions involve several material parameters: the London penetration depth,  $\lambda_L$ , the coherence distance,  $\xi_0$ , the Fermi velocity,  $v_F$ , and the electron mean free path,  $\Lambda$ . Computer programs have been written to evaluate the BCS surface resistance [31]. Calculations from the theories agree well with experimentally measured  $R_s$ .

### 6.1. Niobium

The exponential temperature dependence in the surface resistance due to the energy gap ( $\Delta = 1.9kT_c$ ) is quite

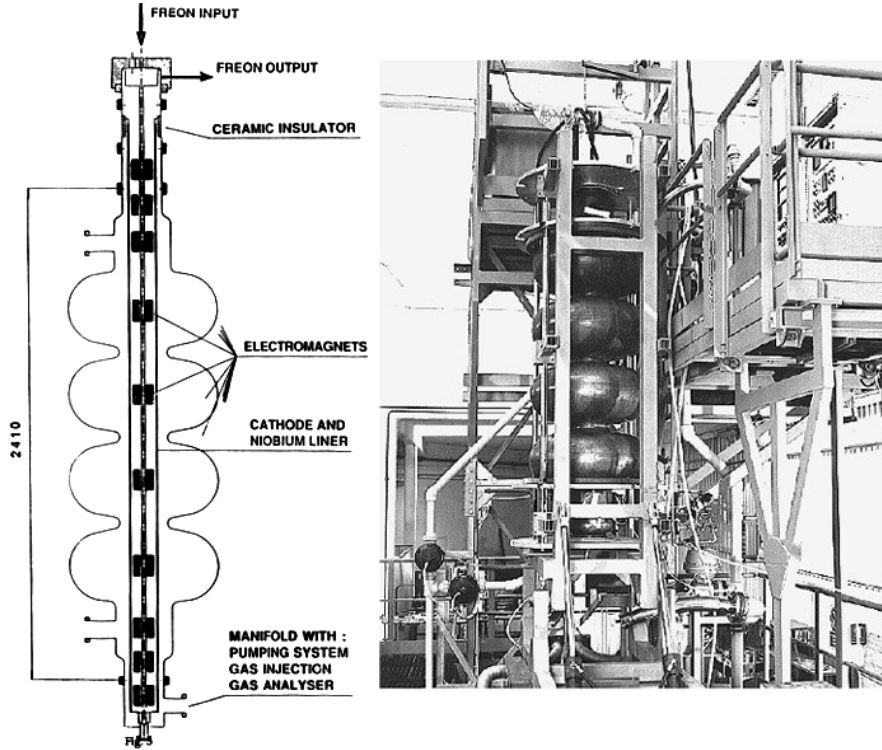


**Figure 13.** Cylindrical magnetron sputtering set-up for depositing niobium on a copper cavity. Electromagnets are placed inside a tube of niobium, which is the sputtering target. Cells are coated one at a time.

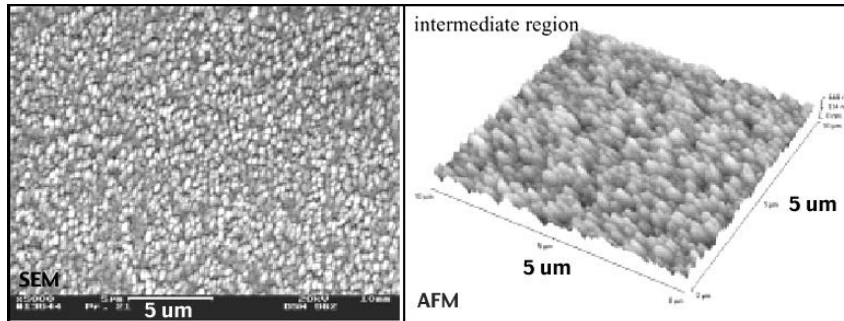


**Figure 14.** Microstructure of a sputtered niobium film using (a) TEM and (b) AFM. The grain size is 100–200 nm, as compared to the greater than  $50 \mu\text{m}$  grain size for sheet Nb. The scale bar in (a) is  $5 \mu\text{m}$  long.

clear from the measured surface resistance of a niobium cavity (figure 16). The frequency dependence of the surface resistance for Nb is shown in figure 17. Note that, for a two orders of magnitude increase in the RF frequency, the surface resistance increases by approximately four orders of magnitude. The small departure from the exact square law arises from the anisotropy of the pairing energy, which is related to the anisotropy of the niobium crystal lattice.

For clean Nb, in the limit of infinite  $\Lambda$ , the intrinsic microscopic parameters are  $\xi_0 = 64 \text{ nm}$  and  $\lambda_L = 36 \text{ nm}$ . The effective coherence length ( $\xi$ ) and the effective penetration depth ( $\lambda_e$ ) depend on the purity, via the electron mean free path  $\Lambda$ , as follows [32]:

$$\xi = \frac{\xi_0 \Lambda}{\xi_0 + \Lambda} \quad \lambda_e = \lambda_L \sqrt{\frac{\xi_0}{\xi}}.$$

For sheet Nb with  $RRR = 300$ , the bulk  $\Lambda = 900 \text{ nm}$ , so

that the  $GL$  parameter  $\kappa = \lambda/\xi = 0.62$ . High-purity bulk Nb behaves as a type I superconductor, but as the  $RRR$  decreases, Nb becomes type II when  $\kappa$  becomes greater than 0.7 at an  $RRR$  below 150. An interesting effect of the mean free path on the surface resistance is shown in figure 18. Note how there is a minimum in the surface resistance when the mean free path becomes comparable to the coherence length.

## 6.2. Nb/Cu

At low fields, the BCS surface resistance of Nb/Cu cavities is lower than for bulk niobium cavities at the same RF frequency. This is primarily due to the effect of the mean free path on the surface resistance. Due to the small grain size, high sputtered gas content and some oxygen content of the films, the mean free path of the sputtered Nb layer is lowered to 30–60 nm, corresponding to a  $RRR$  of 10–20 [34]. This is in the range where the BCS surface resistance

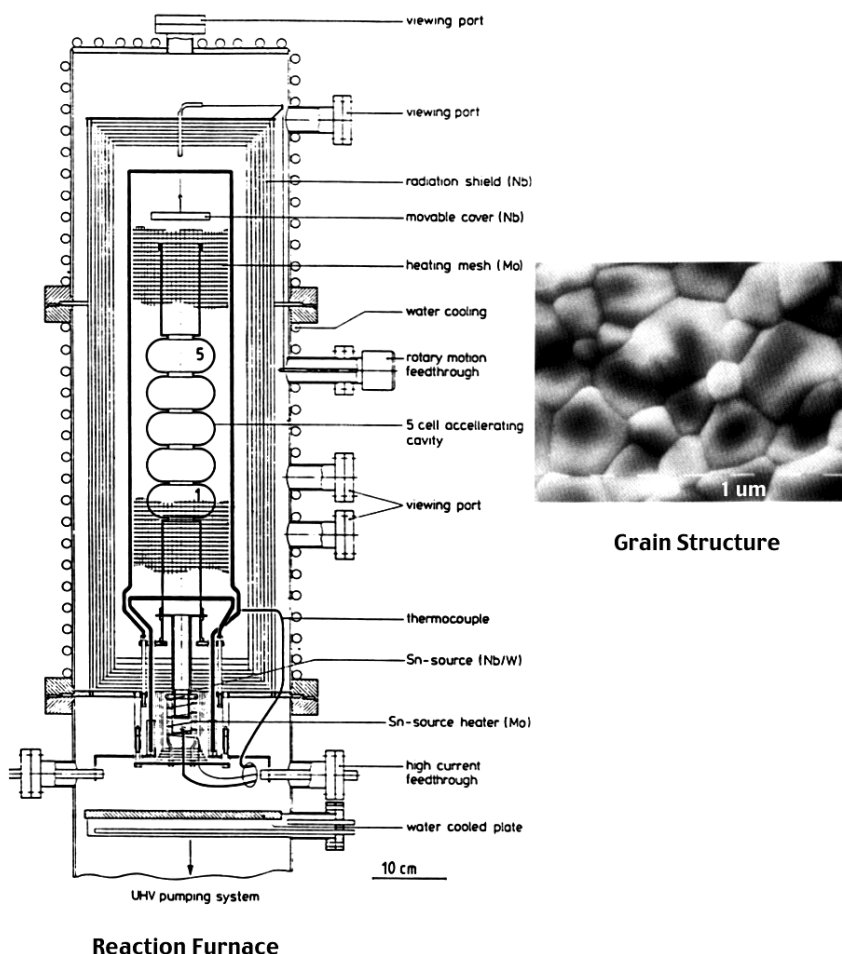


**Figure 15.** (a) Fabrication of  $\text{Nb}_3\text{Sn}$  by solid-state diffusion in a furnace. (b) SEM micrograph of reacted film showing a grain size of  $1\text{--}2\ \mu\text{m}$  [28].

reaches a minimum. Figure 19 shows the variation in the surface resistance of sputtered Nb films when  $\Lambda$  is intentionally changed by using different species of sputtering gas, which results in different amounts of gas burial. The measured energy gap is  $\Delta = 1.87kT_c$ , similar to bulk Nb. Using the simple relationships for coherence length and penetration depth in terms of the mean free path we estimate that the  $\kappa$  value of sputtered Nb is between 1.7 and 3, well into the type II regime. A nagging problem with Nb/Cu films—commonly referred to as the  $Q$ -slope problem—is that the surface resistance depends on the RF magnetic field. A compilation of data [27] shows in figure 20 how the slope depends on the RF frequency.

### 6.3. $\text{Nb}_3\text{Sn}$

Figure 21 shows the temperature dependence of the surface resistance for  $\text{Nb}_3\text{Sn}$  [36]. It fits the BCS theory with  $\Delta/kT_c = 2.2$ ,  $\xi_0 = 6\ \text{nm}$ ,  $\lambda_L = 60\ \text{nm}$  and  $\Lambda = 1\ \text{nm}$ .  $\text{Nb}_3\text{Sn}$  is therefore a strong type II superconductor with  $\kappa = \lambda/\xi \approx 10$ . Below  $T < 0.7T_c$ , the BCS surface resistance of  $\text{Nb}_3\text{Sn}$  can be conveniently described by

$$R_{BCS} = 9.4 \times 10^{-5} \frac{f^2}{T} e^{-2.2T_c/T}.$$

### 6.4. HTSs

As mentioned earlier, there is a large anisotropy of the magnetic and electrical properties between the  $c$ -axis and the  $ab$ -planes, with superior behaviour when the current flow is in the  $ab$ -plane. To produce good quality HTS films, it is therefore necessary to orient the grains so that the  $c$ -axis is normal to the RF surface everywhere. For the HTSs, the coherence lengths are very short: 1.7 nm within the copper-oxygen ( $ab$ ) planes and 0.3 nm perpendicular to the planes, respectively. The effective penetration depths are also very large  $\approx 200\ \text{nm}$  in the  $ab$ -plane and 1000 nm in the  $c$ -direction. YBCO is therefore an extreme type II superconductor with  $\kappa = \lambda/\xi \approx 100$ . Because of these parameters, the ideal part of the superconducting surface resistance is expected to be very high. Figure 22 [37] shows the temperature dependence and figure 23 shows the frequency dependence of HTS films prepared by various laboratories and by various methods.

## 7. Residual resistance

### 7.1. Niobium

Figures 16 and 17 show some of the lowest  $R_0$  values measured over a range of frequencies. Typical  $R_0$  values for Nb cavities

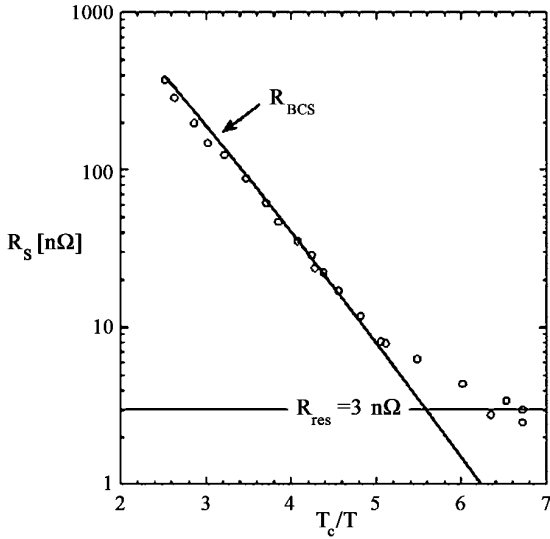


**Figure 16.** Measured temperature dependence of the surface resistance of a Nb cavity at 1.3 GHz. In this semi-log plot, the linear region gives an energy gap of  $\Delta = 1.9kT_c$ . The residual resistance is 3 nΩ.

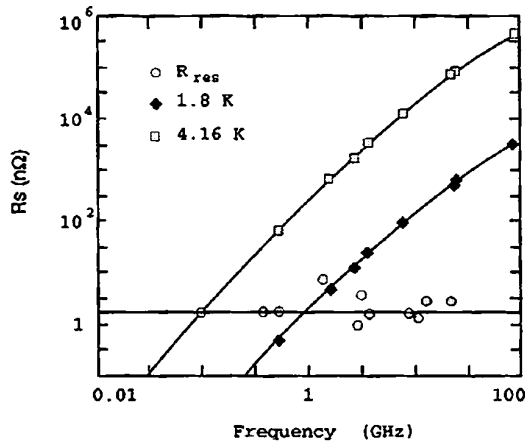


**Figure 17.** Frequency dependence of the surface resistance of Nb. Note the departure from a square law at high frequencies, indicative of the anisotropy in the energy gap. Also note that the residual resistance is nearly independent of frequency [33].

fall in the 10 nΩ range. The record for the lowest surface resistance is 1–2 nΩ.

A well understood and controllable source of residual loss is trapped dc magnetic flux from insufficient shielding of the Earth’s magnetic field or other dc magnetic fields in the vicinity of the cavity, such as stray fields from accelerator magnets. Under ideal conditions, if the external field is less than  $H_{c1}$ , the dc flux will be expelled from the bulk of a superconductor due to the Meissner effect. However, if there are lattice defects or other inhomogeneities in the material, the dc flux lines can be ‘pinned’, and trapped within the material. Surprisingly, experimental studies show that when niobium cavities are cooled down in the presence of a small dc magnetic field (e.g. less than 1 Oe) all the flux within the volume of the cavity is trapped [38]. It is suspected that the oxide layer on the niobium surface serves as a source for flux pinning sites. The flux comes through the cavity wall in current vortices which contain single quanta of magnetic flux. The normal cores of

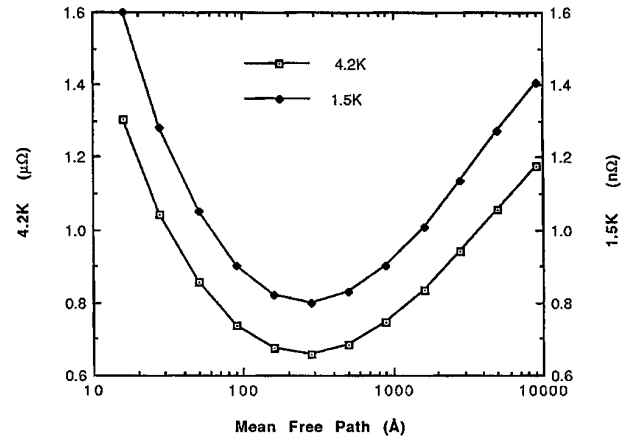


**Figure 18.** Dependence of the BCS surface resistance (at 1500 MHz) on the electron mean free path for Nb. Calculations are shown for two different temperatures, determined from Halbritter’s program for BCS resistance [31].

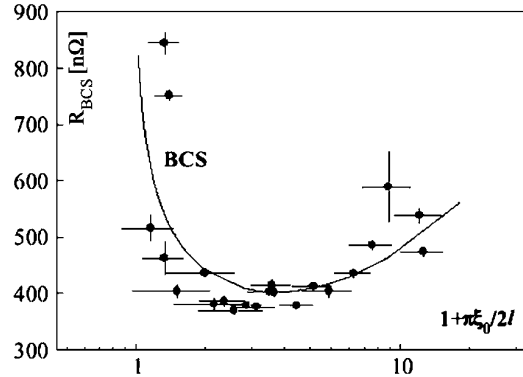


**Figure 19.** A comparison between the measured surface resistance of Nb/Cu films with the predictions from the BCS theory. The mean free path is varied by changing the sputtering gas species [35].

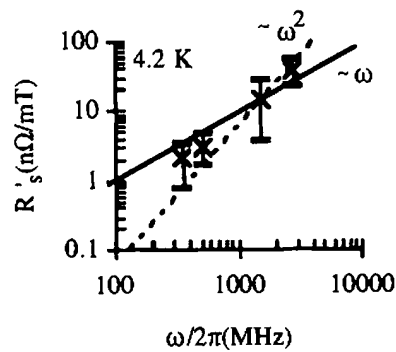


**Figure 20.**  $Q$ -slope for Nb/Cu cavities at various frequencies.

size  $\xi$  cause residual resistance. In RF fields the flux lines oscillate, causing additional losses. Typically, at 1 GHz,  $R_0$  is  $1 \mu\Omega \text{ Oe}^{-1}$ . These losses increase as  $\sqrt{f}$ , where  $f$  is the RF frequency. To obtain the highest  $Q_0$ , a superconducting cavity must therefore be well shielded from the Earth’s magnetic field. If a 1 GHz superconducting cavity is not shielded from the Earth’s field, the maximum  $Q_0$  will be limited to below  $10^9$ .

Another important residual loss mechanism arises when any hydrogen dissolved in the bulk niobium precipitates as a lossy hydride at the RF surface [39]. This residual loss

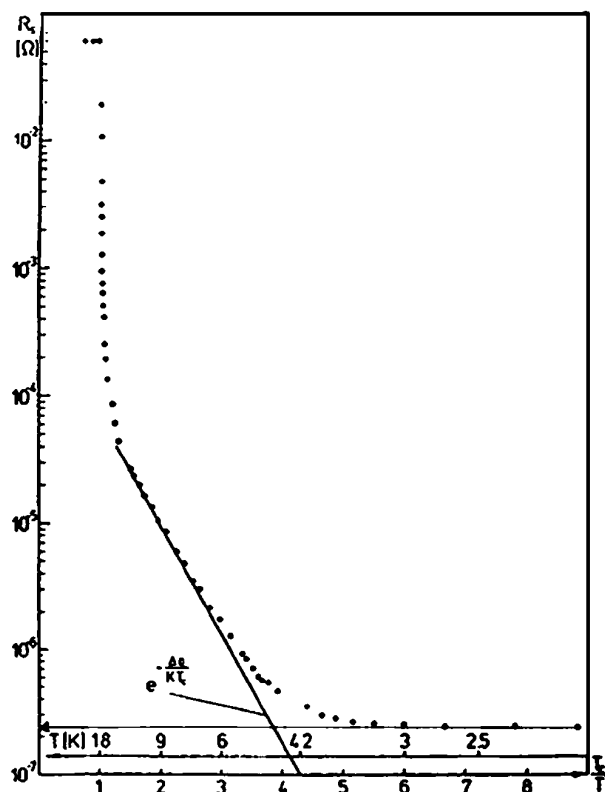


**Figure 21.** Measured surface resistance of a Nb<sub>3</sub>Sn cavity at 8 GHz [36].

(come to be known as the ‘*Q*-disease’) is a subtle effect that depends on the rate of cool-down and the amount of other interstitial impurities or atomic size defects present in the niobium. The disease can be severe enough to lower the  $Q_0$  to  $10^7$ , depending on the amount of hydrogen dissolved and the cool-down rate of the cavity. More than 2 ppm wt of hydrogen can be dangerous. Since one of the methods whereby niobium becomes contaminated with hydrogen is during chemical etching, it is important to keep the acid temperature below 15 °C during the chemical treatment to reduce the generation and absorption of H. A cavity which is contaminated with H can be cured by heating in a vacuum of better than  $10^{-6}$  Torr at 800 °C for 1–2 h, which is sufficient to degas the H from the bulk.

### 7.2. Nb/Cu

At low fields, residual resistance values comparable to niobium have been achieved. To achieve low residual resistance, one of the important parameters for Nb/Cu films is the type and amount of sputtering gas buried in the film. Figure 24 shows the residual resistance ( $R_0$ ) for various sputtering gas species. Krypton is the best both for low residual resistance and low  $Q$ -slope. Other important parameters are the smoothness and purity of the copper substrate. As the average incidence angle of the sputtered Nb is about 15°, reaching up to 50° near the iris, irregularities of the substrate induce film inhomogeneities in their shadow. Starting with a substrate surface that is made very smooth by electropolishing gives the best results. Taking a hint from this behaviour, it is possible that techniques which

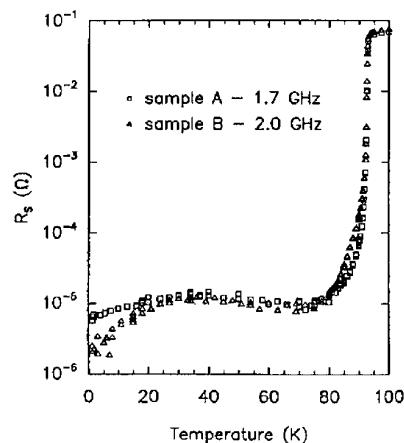


**Figure 22.** Measured temperature dependence of the surface resistance of a high-quality HTS film [37].

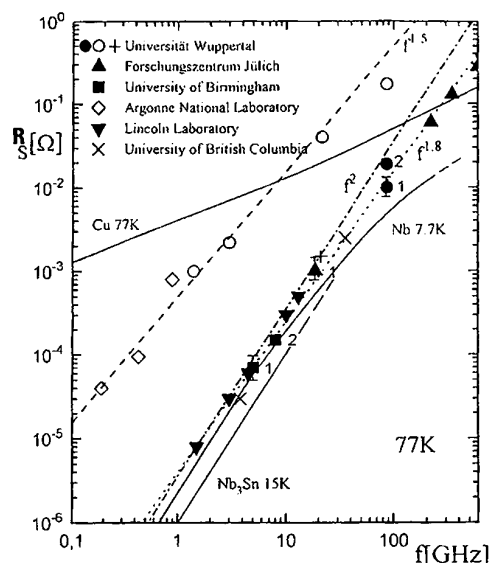


**Figure 23.** Frequency dependence of the surface resistance of high-quality HTS films compared with the surface resistance of Nb, Nb<sub>3</sub>Sn, Cu and a bulk HTS sample. The results for Nb and Nb<sub>3</sub>Sn are presented at 7.7 and 15 K respectively so as to correspond to the same reduced temperature as 77 K for the HTS. The HTS materials are near their residual resistance values at 77 K, and therefore do not improve much at lower temperatures. However, the surface resistance for both Nb and Nb<sub>3</sub>Sn still improves at lower temperatures to residual resistances of  $10^{-8}$  Ω or less [37].

further improve the smoothness of the deposited film may give even better results. There are results which show that the residual losses of Nb/Cu films increase with RF frequency, with a power law between linear and square (figure 18). A frequency dependence suggests that intergrain losses may play a role.

An advantage of thin niobium films on copper is the relative insensitivity of the residual resistance to dc magnetic fields, as compared to niobium. The insensitivity reduces the amount of shielding necessary against the ambient dc magnetic field; but the cause for the resilience of Nb/Cu to dc magnetic field induced losses is not yet understood. The higher  $\kappa$  value of Nb/Cu films and the accompanying higher  $H_{c2}$  could be one contribution. With fewer dc flux centres, the overall

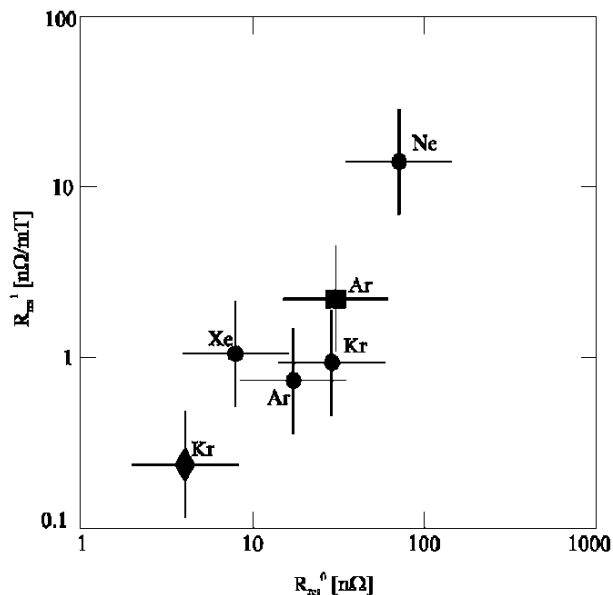


**Figure 24.** Residual surface resistance measured on Nb films sputtered with various gas species. The horizontal axis shows the residual resistance while the vertical axis shows the magnitude of the  $Q$ -slope (section 7.2).

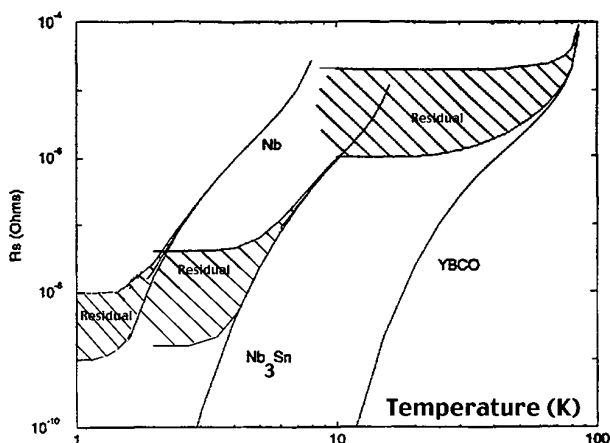


**Figure 25.** A comparison of the surface resistances for various superconductors. Nb is clearly superior to the others. Much improvement remains necessary for the HTSs.

normal state resistance is reduced. However, the increase in  $\kappa$  predicted from the mean free path is quite small. Another contribution could come from the reduced flux flow caused by the large density of pinning sites [26], but this mechanism is discounted in [40].

### 7.3. $Nb_3Sn$ and HTS

Measurements by various laboratories on cavities ranging in RF frequency from 500 to 8000 MHz indicate that the residual losses of both materials increase as the square of the frequency [36, 37]. This may be characteristic of intergrain losses and weak coupling between grains. Figure 25 compares the residual resistance regimes for the various superconductors [32]. Clearly results with solid Nb or sputtered Nb are the best to date.

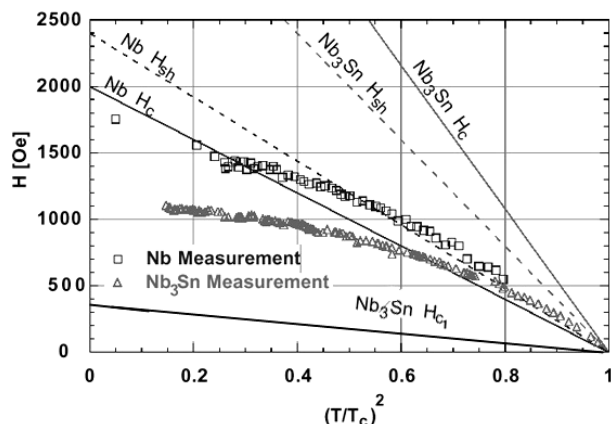


**Figure 26.** Measured RF critical field of Nb and  $Nb_3Sn$  cavities [42].

## 8. High-field behaviour

### 8.1. Fundamental limits—the RF critical magnetic field

As we mentioned, because of nucleation requirements for magnetic flux lines [41], the ‘superheated’ superconducting state persists metastably above  $H_c$  (for type I superconductors) and above  $H_{c1}$  (for type II). Figure 26 shows the results of special experiments aimed at measuring the RF critical fields for Nb and  $Nb_3Sn$  [42]. These experiments use high-power pulsed RF, so that the rise time of the field is shorter than the growth time of normal conducting regions. Thus it becomes possible to exceed the thermal breakdown field and approach the RF critical field.

For Nb, it was possible to exceed  $H_c$ , and to approach the expected  $H_{sh}$ . For  $Nb_3Sn$  it was possible to exceed  $H_{c1}$ , but results fall short of  $H_{sh}$ . It is not known whether this reflects a fundamental difficulty for high- $\kappa$  type II superconductors, or whether the quality of the films prepared limited the attainable field.

### 8.2. Bulk Nb cavities at high fields

Well below the RF critical field, thermal breakdown of superconductivity can originate at submillimetre-size regions of high RF loss, called defects. Typical examples of defects located by temperature mapping are: chemical stains, foreign metal inclusions, pits with sharp edges, metal burrs from scratches, voids or delaminated regions of Nb and welding mistakes. The latter can be loosely bound spatter beads, incomplete weld penetration or dirt inclusions in the melt zone. When the temperature of the good superconductor outside the defect exceeds the superconducting transition temperature,  $T_c$ , the losses increase and large regions become normal conducting. Because the field falls abruptly, we refer to the rapid loss of stored energy as a ‘quench’. Some defects can be superconducting at low fields—for example weakly attached Nb beads from weld spatter. When these regions become normal conducting, there is usually a  $Q$ -switch at low fields, i.e. a drop in  $Q$  by a significant factor, but not all the way down to the normal conducting state. As the field increases,  $Q$  continues to drop, till eventually there is a complete quench.

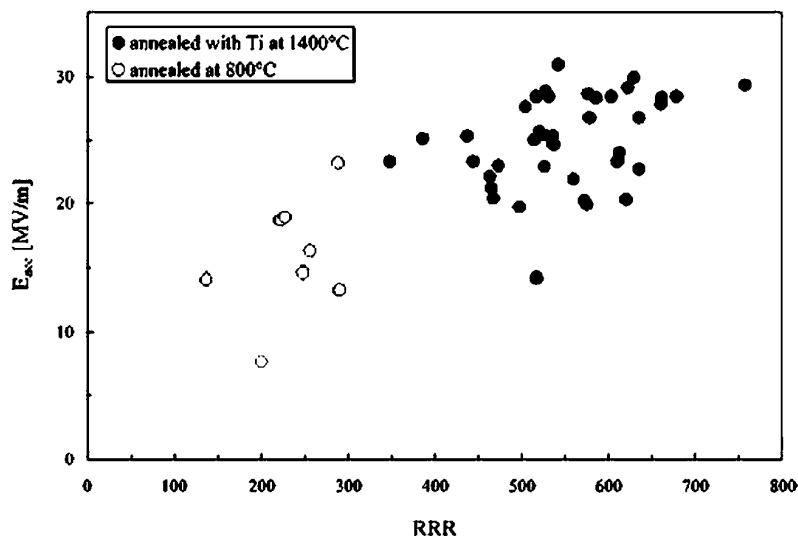


**Figure 27.** Performance improvement with increasing  $RRR$ . For the highest  $RRR$  values many cavities were limited by the available RF power for the test, i.e. they did not quench.

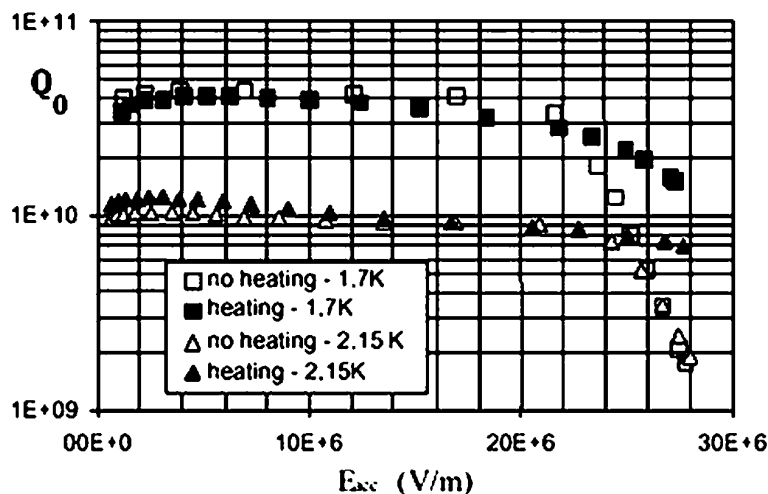


**Figure 28.** Chemically etched cavities that show a high-field  $Q$ -slope. Two test results on a single-cell 1.3 GHz cavity prepared by chemical etching: the open squares denote preparation without baking and the full squares denote preparation after baking. [48].

A simple thermal model predicts that [43]

$$H_{pk} [\text{A m}^{-1}] = \sqrt{\frac{4\kappa(T_c - T_{bath})}{aR_n}}.$$

Here  $a$  is the defect radius,  $R_n$  is the defect resistance and  $\kappa$  is the average thermal conductivity between the operating temperatures  $T_{bath}$  and  $T_c$ . For example, a  $50 \mu\text{m}$  radius defect with  $R_n = 10 \text{ m}\Omega$  will break down at  $H_{pk} = 820 \text{ Oe}$ , if the  $RRR$  is 300, i.e. the average  $\kappa = 75 \text{ W m}^{-1} \text{ K}^{-1}$  at 4.2 K.

An obvious approach to avoid quench is to prepare the niobium material with great care so as to keep it free from defects. Substantial performance gains are experienced from searching the starting niobium sheet for defects by the eddy-current scanning method. However, it is impossible to ensure that there will be no defects, especially in large-area cavities or when dealing with hundreds of cavities. The best insurance against thermal breakdown is to raise the thermal conductivity of the niobium. Then defects will be able to tolerate more

power before driving the neighbouring superconductor into the normal state. The most effective approach to increasing the thermal conductivity of niobium is to remove the interstitial impurities, chiefly oxygen, nitrogen and carbon. These impurities are volatile only near the melting temperature of niobium. Therefore the best purification method is to improve the electron beam melting technique and the conditions for refining the starting ingot at the niobium producing plant. Figure 8 shows how the thermal conductivity of Nb increases with increasing purity, most conveniently characterized by the  $RRR$  of Nb.

Another technique for improving niobium purity is solid-state gettering using yttrium [44] or titanium [45]. These metals have higher affinities for oxygen than Nb. A Nb cavity or half-cell is coated with the gettering metal and heated for several hours to a high temperature, for example,  $1200^\circ\text{C}$  for yttrium or  $1350^\circ\text{C}$  for titanium. At these temperatures the interstitial impurity atoms are quite mobile. When they arrive at the surface they sink into the foreign metal coating.

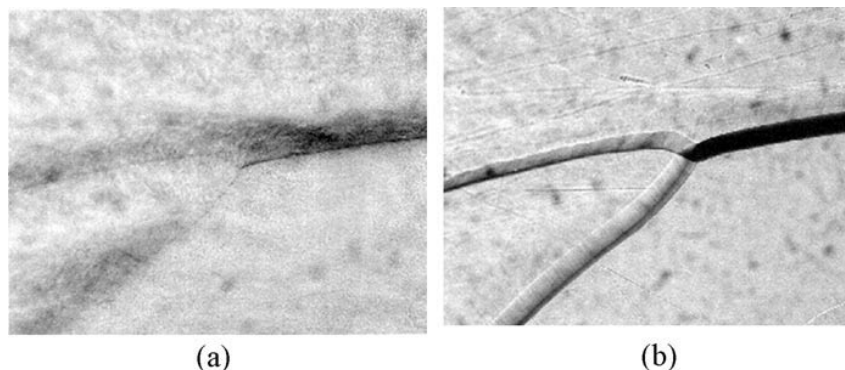


**Figure 29.** Expanded optical micrographs of grain boundaries in the welded regions. The typical grain size is 1 mm. (a) Electropolished to remove 100  $\mu\text{m}$ , (b) after standard chemical polishing to remove 44  $\mu\text{m}$ . Note that in (a) electropolishing still leaves a grain boundary step, although it is not as high, nor as sharp, as the step that results from standard chemical etching [23].

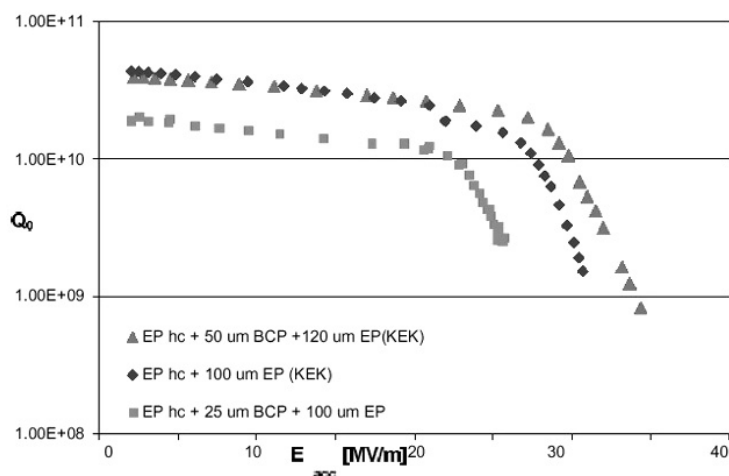


**Figure 30.** Results on single-cell, 1.3 GHz cavities prepared by electropolishing at CERN. Note that although there is a  $Q$ -slope, the onset (usually 25–30  $\text{MV m}^{-1}$ ) is generally higher than for chemical etching (usually, 20  $\text{MV m}^{-1}$ ). The quench field, 30–40  $\text{MV m}^{-1}$ , is also higher than for chemical etched cavities [51].

Both coating and purification operations can be combined into one step because, at the diffusion temperature, the vapour pressure of the getter metal is also high enough to evaporate the necessary layer. The high-temperature treatment removes nearly all of the dominant oxygen impurity. After the purification operation, the getter material and the underlying compound layer are chemically etched away. Commercial niobium of  $RRR = 250\text{--}300$  has been improved to  $RRR = 500\text{--}700$ . Since the vapour pressure of titanium is lower than that of yttrium, higher temperatures or longer times are needed with titanium. However, titanium does have the intrinsic capability to remove nitrogen and carbon by solid-state gettering because of its appreciable affinity for these impurities. Since the diffusion rates of nitrogen and carbon are much lower than the rate of oxygen, very long gettering times are necessary. Using titanium for more than 50 h, an  $RRR$  of 1000 was achieved in samples of starting  $RRR = 200$  [46].

The post-purification must be done after the half-cell forming stage, or with a complete cavity, because grain growth at the high temperature will destroy the mechanical workability of niobium, making it impossible to form the cavity if the sheet is purified first. Since, at 1350  $^{\circ}\text{C}$ , titanium diffuses into niobium to a substantial depth (100  $\mu\text{m}$ ) along the grain

boundaries, heavy chemical etching becomes necessary after the post-purification step. The outside surface of a cavity must also be etched by about 50  $\mu\text{m}$  to re-establish good heat transfer at the cooling surface.

The benefits of high- $RRR$  Nb on the gradient of Nb cavities can clearly be seen from the performance of TTF cavities, as shown in figure 27 [16]. Here the measures taken to increase  $RRR$  have been coupled with efforts to avoid defects by prescreening the material and to avoid field emission by high-pressure rinsing, as discussed below. For the high-temperature, post-purified cavities, the effective  $RRR$  could be even higher than the plotted numbers because the material near the RF surface has a substantially higher  $RRR$  than the bulk [19]. The results shown in figure 27 carry substantial weight since they were obtained with a large number of nine-cell cavities, each with an area of about 1  $\text{m}^2$ . Due to the large area, the probability of encountering defects that could lead to quench is quite significant. Single-cell results may not appear as sensitive to  $RRR$  because with the extra care possible for small cavities and their small area it is easier to avoid defects and consistently reach high fields.

High- $RRR$  niobium has some negative effects. High-purity niobium cavities are more sensitive to  $Q$  degradation

from hydrides because H is more mobile in the absence of interstitial impurity atoms that serve as trapping centres (see [7]). High-temperature solid-state gettering also lowers the yield strength of the material. Appropriate measures must be taken to avoid collapsing a thin-wall cavity whose yield strength is lowered by purification. All in all, it would be much better to obtain high-RRR, high-strength sheet metal directly from industry, and to avoid the high-temperature process and its needed post-treatments altogether. Past experience suggests that this should be possible by improving the residual gas pressure in the industrial electron beam melting furnace.

## 9. High-field $Q$ -slope

Now that thermal breakdown is under better control, there is a strong push toward the ultimate field,  $H_{sh}$ . Unfortunately, there are two known hurdles in the road. One is field emission, which, as we will discuss in section 10, is well understood and reasonably under control. The other is a less understood phenomenon called the ‘high-field  $Q$ -slope’. Techniques to bring it under control are just being explored.

In one-cell and two-cell cavities tested at various laboratories [47–49], there is a steady decline in  $Q_0$  observed above 20 MV m<sup>-1</sup>, followed by a quench (see figure 28). All this occurs in the absence of field emission (no x-rays detected). Temperature maps reveal that the power dissipation occurs over large sections where the magnetic field is high.

One mechanism proposed for the high-field  $Q$ -slope [49] is magnetic field enhancement at surface microstructures, such as grain boundaries. Figure 12 compares micrographs of chemically polished and electropolished regions [23]. Surface profiling shows that most steps are about 5  $\mu\text{m}$  in height. In the extreme, 12  $\mu\text{m}$  steps with slope angles of the order of 20° are possible. Electromagnetic field calculation codes determine the extent of field enhancement to be between 1.2 and 1.8 for chemically etched Nb [49].

According to the ‘roughness model’, the  $Q$ -slope begins when, around the average field of 20 MV m<sup>-1</sup> (800 Oe), the steepest grain boundary structures exceed the RF critical field due to the geometric field enhancement. Heat flow simulations show that a quench along an isolated boundary does not evolve into a global quench, but results only in increased dissipated power, i.e. a reduced  $Q$ . As more and more grain boundaries quench with increased field, the  $Q$  drops further. Eventually, around 30 MV m<sup>-1</sup>, thermal breakdown occurs when the heat flux at the He interface exceeds the critical flux at the Nb–He interface. This steady progression of quenching grain boundaries provides a quantitative fit for the high field  $Q$ -slope. In the roughness model the  $Q$ -slope arises primarily from the normal conducting resistance of the quenched grain boundary edges.

Recrystallized grains along electron beam welds (figure 29) are likely to accentuate the  $Q$ -slope effect because the grains in the melted region are longer (millimetres) and show a larger step height (30  $\mu\text{m}$ ). Also, grain boundaries in the equator weld region are predominantly oriented perpendicular to the RF magnetic field, leading to a larger average field enhancement [23]. Therefore cavities

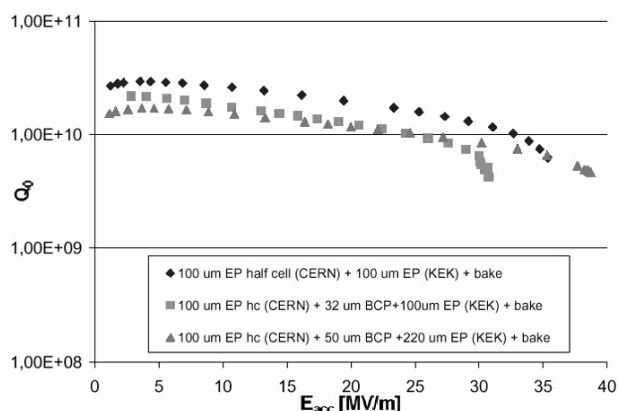


**Figure 31.** Results of single-cell cavities prepared by electropolishing and baking at CERN. Note the absence of the high-field  $Q$ -slopes up to 28 MV m<sup>-1</sup>, and quench fields above 30 MV m<sup>-1</sup> [51].

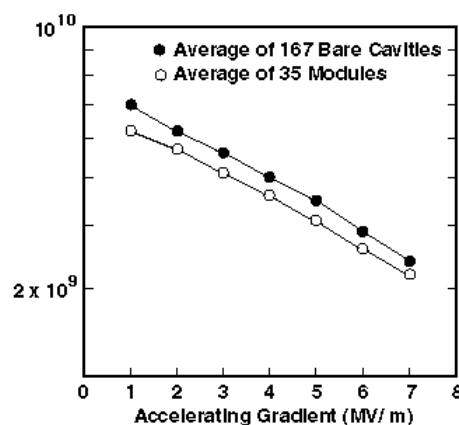


**Figure 32.**  $Q$ -slope behaviour endemic to Nb/Cu cavities shown by hundreds of 350 MHz cavities prepared for LEP-II [35].

suffering from a strong  $Q$ -slope are likely to quench near welds, as is often observed.

If the geometric field enhancement model is correct, any cavity preparation or surface treatment procedure that produces roughness is likely to lead to a  $Q$ -slope. For example, recent experience on spinning single-cell cavities from a single sheet resulted in an inner surface with a large crack density and significant  $Q$ -slope [50]. Removal of fissures by mechanical and other polishing methods reduced the  $Q$ -slope. Magnetron sputtered Nb has fine grains with roughness on the submicrometre scale. This may well be the leading cause of the  $Q$ -slope endemic to Nb/Cu cavities, which starts at low fields.

Conversely, any treatment that increases smoothness reduces the  $Q$ -slope. It is clear from the micrographs (figure 12) that electropolished surfaces are smoother; but mild steps are still present at grain boundaries. Therefore the field enhancement factors at grain boundaries are lower with electropolishing. There is now substantial evidence from several laboratories [48, 50–52] to support that an electropolishing treatment increases the onset field level of the  $Q$ -slope as well as the final quench field level. For an electropolished surface the  $Q$ -slope begins around 25–

27 MV m<sup>-1</sup>, ending with a quench between 30 and 35 MV m<sup>-1</sup> (figure 30). This is an improvement over the typical  $Q$ -slope onset field of 20 MV m<sup>-1</sup> for a Nb surface prepared by standard chemical etching, followed by quench at 25–30 MV m<sup>-1</sup>.

There is not yet agreement that the grain boundary field enhancement mechanism is responsible alone for the high-field  $Q$ -slope. The issue remains open because there is another cavity treatment which improves the high-field  $Q$ -slope of both chemical etched and electropolished cavities. This is the baking of a cavity under vacuum between 85 and 140 °C for periods of 40–50 h and longer. It is unlikely that such baking will modify the local geometry. Therefore magnetic field enhancement from changes in the surface roughness cannot be the sole mechanism for the  $Q$ -slope. Figure 28 shows a clear improvement in the  $Q$ -slope of a cavity prepared by chemical etching and followed by baking. Similarly, figure 31 shows that baking results in a substantial improvement of the  $Q$ -slope of the electropolished cavities of figure 30 [51]. Accelerating fields up to 40 MV m<sup>-1</sup> without significant  $Q$ -slope have now been reached at two laboratories using electropolishing plus baking [51, 52] as shown in figure 31.

What properties does baking change? One result of the bake—known for quite some time—is that the mean free path of the RF layer decreases due to the break-up of the oxide layer and the subsequent diffusion of oxygen from the oxide layer into the RF layer. XPS spectra of niobium heated to 200 °C [53] showed surface oxide dissolution. When a 1.3 GHz cavity is baked at 100–140 °C for 40–50 h, the BCS surface resistance decreases by about a factor of two [54]. As shown in figure 18, a large part of this decrease in surface resistance arises from the drop in the mean free path.

At first glance it may appear that the drop in the BCS surface resistance could account for the reduction of the  $Q$ -slope; but the decrease of BCS resistance is only a factor of two, whereas the observed change in  $Q$  in the high-field region is a factor of five. Why does baking alter the high-field  $Q$ -slope and the quench field? A possible explanation [55] is that the bake alters the microscopic parameters of the RF layer sufficiently to raise the RF critical field by the order of a few per cent. Perhaps the RF critical field depends on the mean free path, an interesting possibility worth exploring on theoretical grounds. The drop in mean free path is already a confirmed effect from the drop in the BCS resistance. Together with the grain boundary field enhancement model, the increased RF critical field would allow both an increase in the quench field and a reduction in the  $Q$ -slope. Yet an increase in the RF critical field with increased oxygen content would be puzzling, in view of the well known effect that  $T_c$  drops with oxygen impurity as well as the BCS prediction that  $H_c \approx T_c$ .

### 9.1. Nb/Cu at high fields

The  $Q$ -slope problem already appears at low fields for a Nb/Cu cavity. The surface resistance starts to increase with  $E_{acc}$ , as seen by the exponential drop in  $Q_0$  (figure 32). The cause is not yet fully understood, but surface roughness could also be operative here. There is a strong correlation between residual losses and the  $Q$ -slope as evident from figure 24. AFM micrographs (figure 14(b)) show severe roughness on the micrometre scale. Experience shows that lowering the

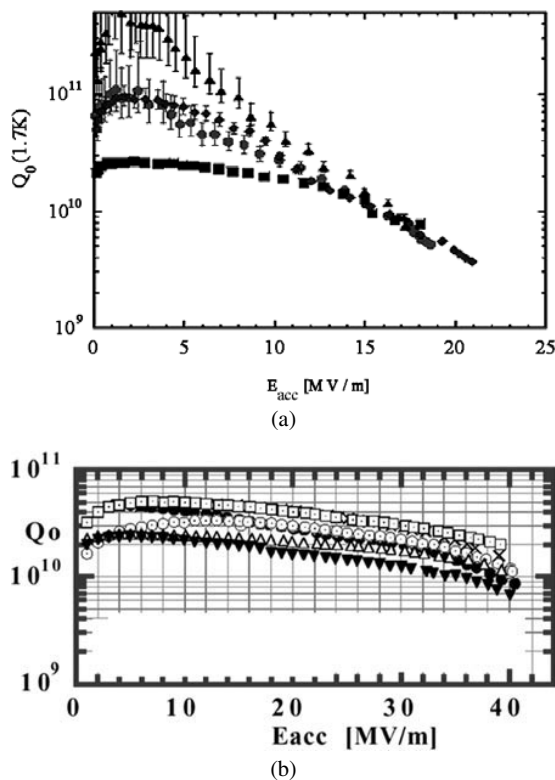


**Figure 33.** A comparison between the performance of (a) the best Nb/Cu and (b) the best sheet metal Nb cavities at about 1.5 GHz.

roughness from 0.8 to 0.2  $\mu\text{m}$ , for example by controlling the spinning procedure of the copper substrate, gives lower residual resistance and lower  $Q$ -slope. More evidence that roughness is responsible for the  $Q$ -slope comes from results on films deposited on smoother substrate copper cavities obtained by electropolishing; yet, a significant  $Q$ -slope remains, begging explanation. Perhaps smoother films obtained by increasing the deposition energy of the sputtered atoms would reduce the slope further.

Another possibility for the  $Q$ -slope is intergrain losses, a basic effect for fine-grained superconductors. Counter evidence for this mechanism comes from the fact that films grown on oxidized copper have a grain size of 100 nm, but when grown on an oxide-free surface the grain size is of the order of micrometres. However, the  $Q$ -slope does not decrease with the larger grain size. Other possibilities are impurities in the film and surface roughness. Irregularities on the substrate can result in film inhomogeneities.

At present the  $Q$ -slope makes sputtered Nb/Cu unattractive for high-frequency applications, such as TESLA. The highest accelerating field reached at 1500 MHz is 20 MV m<sup>-1</sup> [35], as shown for the single cell cavity in figure 33(a). By comparison (figure 33(b)), single-cell sheet metal Nb cavities have now reached  $E_{acc} = 40$  MV m<sup>-1</sup> [52].

### 9.2. Nb<sub>3</sub>Sn at high fields

The performance of Nb<sub>3</sub>Sn cavities is far below that of niobium cavities, although it must be emphasized that the relative effort devoted to Nb<sub>3</sub>Sn has been far less than for niobium cavities. Figure 34 shows the best performance achieved. The film

was prepared by the solid-state reaction method [28]. The maximum  $E_{pk}$  reached was  $33 \text{ MV m}^{-1}$ , which corresponds to  $E_{acc} = 16 \text{ MV m}^{-1}$  for typical structure parameters. There was no field emission in these tests, and there are regions of substantial  $Q$ -slope. Once again, this strong increase of surface resistance with field is possibly due to roughness from the micrometre-size grain structure (see figure 15) or due to intergrain losses arising from imperfect material embedded between grains.

A characteristic feature of  $\text{Nb}_3\text{Sn}$ -on-niobium cavities is that the  $Q_0$  values are sensitive to the cool-down rate of the cavity through the transition temperature. This is attributed to trapped magnetic flux from thermoelectric currents generated from the temperature differential across the bimetallic  $\text{Nb}/\text{Nb}_3\text{Sn}$  layer [36]. Therefore, when first cooling down the cavities to He temperatures, it is important to cool slowly through the transition temperature, typically at  $10 \text{ K h}^{-1}$ . The low-field  $Q_0$  value has also been observed to drop irreversibly if there is a local thermal breakdown. This effect is again attributed to thermo-currents and the associated magnetic flux generated at breakdown.

### 9.3. HTSs at high fields

Since the discovery of HTSs, the high-field performance has continued to improve steadily as have the techniques to deposit epitaxial films. However, the best films are still not competitive with Nb. From figure 35 it is encouraging to see that the surface resistance stays constant to fields as high as 600 Oe and temperatures as high as 50 K. At these performance levels, however, planar HTS films are attractive only for low-field, passive electronic applications involving planar devices, such as multipole band-pass filters or compact delay lines, but not for high-field accelerator applications [37].

Although we may continue to expect improvements with understanding and better techniques, there may be a fundamental limit to performance arising from the pairing mechanism in HTSs. In superconductors, the energy gap has an angular dependence determined by the angular momentum of the pairing electrons (or holes, for HTSs). For zero angular momentum (s-wave pairing) the energy gap remains finite in momentum space, and without nodes. However, for d-wave pairing, where the angular momentum quantum number  $l$  equals two, the energy gap vanishes at points in certain momentum directions, producing nodes. As a result, a very small amount of energy can excite electrons (holes) out of the paired superconducting state. The ideal surface resistance may not continue to decrease exponentially as for superconductors with s-wave pairing. The surface resistance may reach a fundamental lower limit, possibly as high as  $\mu\Omega$ .

## 10. Field emission

Field emission is a generic problem for all high-voltage devices. Superconducting cavities are particularly sensitive to field emission, because losses from other sources are low. As a result, the SRF community has devoted considerable resources to understanding the origins of field emission and paid a great deal of attention to avoiding field emission and dealing with residual emission.

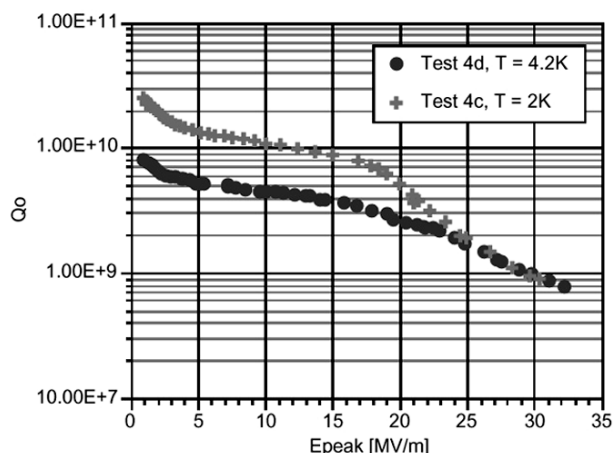


Figure 34.  $Q_0$  against  $E$  for one of the best performing  $\text{Nb}_3\text{Sn}$  cavities [28].

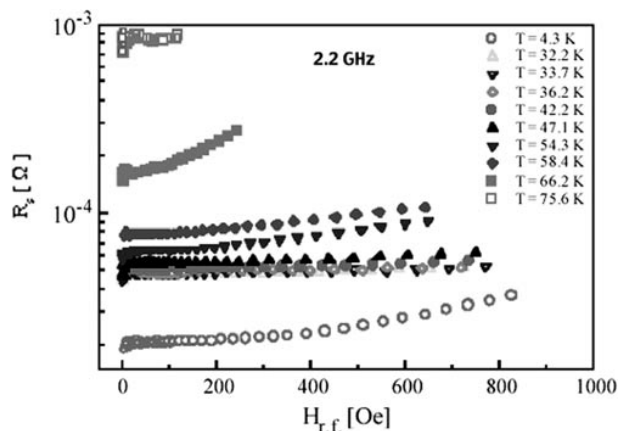
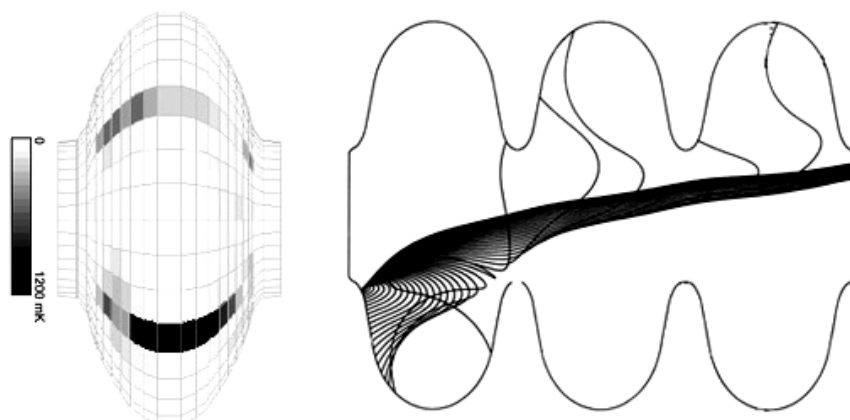


Figure 35. Surface resistance of HTS films with increasing RF magnetic field [37].

At the onset of field emission, the  $Q_0$  of a niobium cavity typically starts to fall steeply because of exponentially increasing electron currents emerging from the surface. The temperature mapping diagnostic technique for superconducting cavities shows that emission always arises from particular spots, called ‘emitters’, usually located in high electric field regions. The electrons that emerge from the emitters travel in the RF fields of the cavity and impact the RF surface (figure 36). Since the power deposited by impacting electrons depends on their trajectory as well as on the intrinsic properties of the emitter, the pattern of temperature rise as a function of position along a given meridian contains implicit information on the location and characteristics of the emission source. By tracking the heating patterns with thermometers, it is possible to locate the emitters and analyse them.

The RF tests are followed by a dissection of the cavity to examine the emitter using surface analytic instruments, such as SEM and EDX. An example emitter is shown in figure 37—a very jagged particle containing titanium, carbon, oxygen, sodium, indium, aluminium and silicon [56]. So far, all emitters have been found to be microparticle contaminants. Similar studies on dc field emission also reveal emitters to be microparticle contaminants. Note that these micrometre-size particles are much smaller than the defects that cause thermal



**Figure 36.** Calculated electron trajectories in a three-cell 1.5 GHz cavity operating at  $E_{pk} = 50 \text{ MV m}^{-1}$ . Here the emitter is located in an end cell, just below the iris, where the surface electric field is  $44 \text{ MV m}^{-1}$ . Note that a significant number of electrons emitted during the early part of the RF cycle bend back and strike the wall near the emitter. On the left is the temperature map from the heating of impacting electrons.

breakdown (typically  $>50 \mu\text{m}$ ). Emitting particles generally have a very irregular shape, and micro-protrusions that enhance the field. Other important factors that influence the emission characteristics are the nature and quantity of condensed matter on the particle, as well as the interface between the particle and the substrate.

The reason for the large spread in the gradients of SRF cavities is the large spread in emitter characteristics, and the random occurrence of microparticle emitters on the RF surface. Accordingly, a high level of cleanliness is always necessary for cavity surface preparation.

### 10.1. Voltage breakdown

When raising the RF electric field in a superconducting cavity for the first time, the field emission often decreases abruptly; the cavity is said to ‘process’ or ‘condition’. Along with the progress in identifying emitters to be microparticles, there has been much progress in characterizing processed emitters using techniques such as SEM, EDX, Auger spectroscopy and AFM. These studies reveal that emitter processing is an explosive event that accompanies what we usually refer to as a ‘spark’ or a ‘discharge’ that occurs during the momentary ‘electrical breakdown’ of the insulating vacuum. Figure 38 shows a typical SEM photomicrograph of an exploded emitter site. There are micrometre-size melted craters surrounded by a  $100 \mu\text{m}$  size starburst feature. Figure 39 shows a field emitting particle of silica intentionally placed in a high electric field region on the surface of a break-apart SRF cavity [57]. After application of an RF electric field of about  $75 \text{ MV m}^{-1}$ , the cavity was disassembled and the site re-examined to show the structures of figure 39 at the particulate site. Note the starburst regions surrounding the melted craters.

Simulations have been conducted to trace how field emission from microparticles evolves into a voltage breakdown that yields the craters and startbursts [58]. The results suggest the following picture. When the electric field increases and the emission current density exceeds a threshold (typically  $10^{11} \text{ A m}^{-2}$ ), the temperature at the emission region becomes high enough to melt a small region of the particle. When the local regions melt they cease to emit, but the overall



**Figure 37.** SEM photomicrograph of a field emitting microparticle found by temperature mapping and subsequent dissection of a single-cell 3 GHz cavity. EDX analysis shows that the particle contains titanium, carbon, oxygen, sodium, indium, aluminium and silicon. Note the very rough surface of the particle. Such protrusions cause geometric field enhancement [56].

emission from the jagged particle continues. The melting of such local regions may be responsible for the instability usually observed in the field emission current. Atoms evaporate from the molten regions to form a cloud of gas around the emission site. Ohmic heating from the emission current can also degas surface adsorbed atoms. The presence of gas surrounding the emitter now starts to play a paramount role in the subsequent stages of intense emission, followed by the eventual explosion of the emitter. Once the field emission current ionizes the gas, the ions return to bombard the emitting surface, causing further gas evolution. Now it is the total emission current that governs the subsequent evolution. The electron and ion bombardment heating can grow intense enough to melt large regions of the emitting particle. The ion current produces secondary ions and electrons, and heats the site further by bombardment, so that more gas is produced. A plasma forms, extending far from the emitter. The electron and ion bombardment from such a plasma cleans the surface to form the starburst feature, which appears dark in the SEM because it is cleaner.

The simulations further show that the more massive ions move slowly relative to the electrons so that a significant

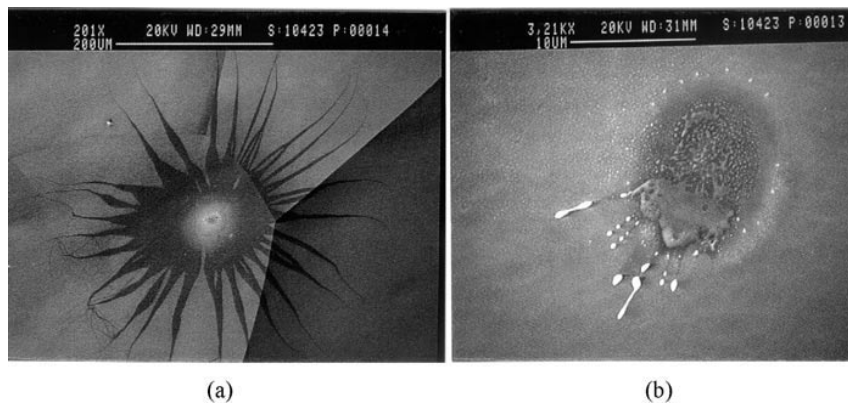


**Figure 38.** SEM photomicrographs of the processed site found at the location predicted via temperature maps; (a) low magnification and (b) high magnification of the crater region within the starburst of (a). The molten splashes in the crater region were found to contain indium, presumably from the indium wire seals used to make vacuum joints.

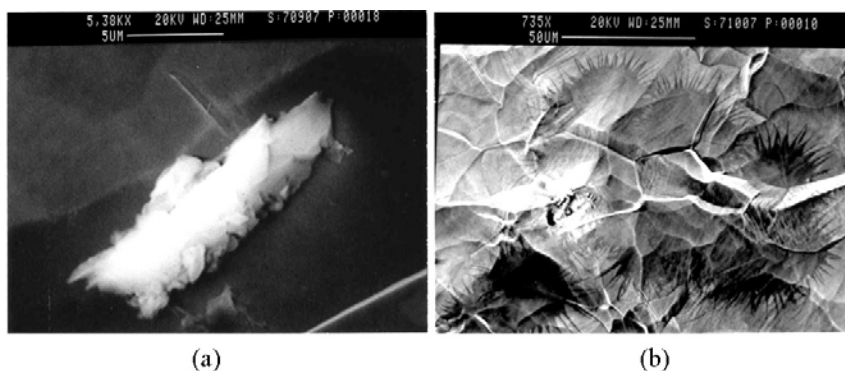


**Figure 39.** (a) SEM photomicrograph of a particle of silica intentionally placed on the surface of a break-apart SRF cavity. Note the jagged nature of the particle. (b) SEM photomicrograph of the silica site after applying an RF field of  $75 \text{ MV m}^{-1}$ . Note the starburst regions.

number of ions begins to accumulate near the emitter. This leads to a substantial electric field enhancement near the emitter. At the emission site the field can approach gigavolts per metre even when the applied RF field is just  $30 \text{ MV m}^{-1}$ . As the field grows, so does the emission current. The current avalanche results in a gas discharge, i.e. an RF spark or an arc. At the core of the arc, the intense current melts niobium, produces molten craters, vaporizes the entire emitting particle and leaves a deposited film of the original contaminant on the crater. In many cases the discharge event leaves behind micrometre-size chunks of molten debris. It is the plasma pressure during the discharge that excavates the molten zone and ejects droplets. There may be multiple arcs between the ion cloud and the niobium, resulting in multiple craters from a single original emission site.

After the explosion, the crater and other melted particles cease to emit at the applied field because they are now smooth particles. Thus voltage breakdown in a RF cavity reduces emission and allows higher electric fields. For a dc, high-voltage gap, however, voltage breakdown can deteriorate the voltage standoff capability because the spark can erode the counter-electrode and deposit more particles.

### 10.2. Overcoming field emission

The field emitter studies discussed above show that increased vigilance in cleanliness during final surface preparation



**Figure 40.** TTF cavity assembly in a class 100 clean room.

and assembly procedures is important to keep particulate contamination and the associated emission under control. Sensitized by these results, new approaches have been adopted to strive for high levels of cleanliness in cavity surface preparation, leading to fewer emission sites and better cavity performance. Figure 40 emphasizes the care and cleanliness necessary during assembly of superconducting cavities in a clean room at the TTF. A technique to further improve

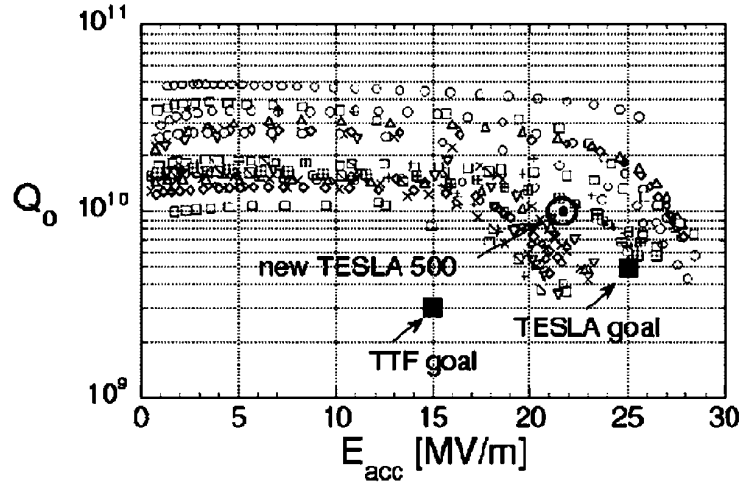


**Figure 41.** High field and high- $Q_0$  performance obtained for many nine-cell 1.3 GHz TTF cavities by pulling together the advances of high-purity niobium, eddy-current scanned Nb sheets, and HPR [12].

cleanliness is high-pressure water rinsing (HPR) [59–61]. A jet of ultra-pure water dislodges surface contaminants that normally resist removal with conventional rinsing procedures. The benefits of HPR in reducing field emission are well demonstrated in tests with nine-cell cavities at DESY [12] as shown in figure 41 where the field emission intensity is sufficiently mitigated so that field levels of 20–30 MV m<sup>-1</sup> are consistently reached.

With the super-cleanliness approach it is clear that field emission can be substantially reduced. However, in large-area structures there is always a significant probability of dust falling into the cavity upon installation of power-coupling devices or during the installation of a cavity into the accelerator. It is clear that a technique to eliminate emitters *in situ* is necessary for the successful application of superconducting cavities in accelerators.

Called high pulse power processing (HPP), such a technique is based on the observation that emitters can be destroyed by the application of high fields. We discussed how field emission extinguishes when the field increases with applied RF power to initiate a voltage breakdown event. The essential idea of high-power RF processing of an emitter is to apply high RF power so as to raise the surface electric field at the emitter as high as possible, even if for a very short time (microseconds). Accordingly, the power level, pulse length and coupling need to be arranged. An important benefit of HPP is that it can be applied to recover cavities that may be accidentally contaminated, for example, in a vacuum mishap. As a result, HPP can be used to reach high gradients in cavities already installed in the accelerator. One example of ‘before-and-after’ HPP is shown in figure 42 [62]. Here a cavity contaminated down to 10 MV m<sup>-1</sup> improves with HPP to 28 MV m<sup>-1</sup>.

A possible concern about the HPP method is the degree to which  $Q_0$  may be degraded by the presence of a large number of destroyed emitters and craters. Another concern is whether the craters may become defects that cause thermal breakdown. Figure 42 shows that the  $Q_0$  does not degrade below  $10^{10}$ . A two-cell, 3 GHz cavity, which was processed by HPP to  $E_{pk} = 70$  MV m<sup>-1</sup>, still showed  $Q_0 = 10^{10}$  at  $E_{pk} = 40$  MV m<sup>-1</sup>, CW. Furthermore, on dissection, more

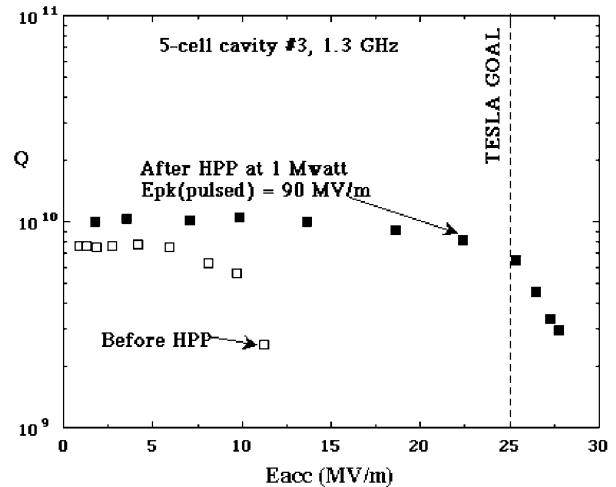


**Figure 42.** Improvement in performance of a five-cell, 1.3 GHz cavity after HPP to process field emitters. With 200  $\mu$ s pulses at 1 MW it was possible to reach a field of 90 MV m<sup>-1</sup> to process emission sites [62].

than 40 starburst-crater areas were found in this cavity [63]. Therefore the large numbers of processed sites do not seriously degrade  $Q_0$  nor create a thermal breakdown problem. This is not surprising, since the molten regions are generally less than 10  $\mu$ m in size so that even a large number of craters do not pose a serious threat. Of course an initial high level of cleanliness is still essential to achieve a low density of emission sites. Also, the processing must be carried out gradually to keep the individual craters from becoming very large.

## 11. Closing remarks

There has been much progress in understanding the gradient and  $Q_0$  limitations in superconducting cavities. Through better understanding new techniques have been developed to overcome the limitations. Producing high gradients and high  $Q_0$  with Nb cavities demands excellent control of material properties and surface cleanliness. As a result of the improved

understanding and the invention of new treatments, there has been much progress in reducing the spread in gradients that arises from the random occurrence of defects and emitters. Prescreening the starting material by eddy-current scanning reduces the number of defects that can cause thermal breakdown. High-RRR, high-thermal-conductivity Nb reduces the impact of any remaining defects. It will be important to aim for higher RRR in large-area cavities, where there is a high chance of defects and contamination. High-pressure rinsing greatly reduces the number of field emitters. HPP destroys accidental field emitter contaminants. This technique will continue to be necessary in order to realize—in accelerators—the high intrinsic gradient potential of SRF cavities. There is now excellent prognosis for reaching  $25 \text{ MV m}^{-1}$  for future colliders. The road to  $40 \text{ MV m}^{-1}$  is opening up. Although the most successful cavities are based on Nb, some exploratory work has been carried out on other materials.

## References

- [1] Padamsee H 1999 *Frontiers of Accelerator Technology* ed S I Kurokawa *et al* (Singapore: World Scientific) p 383
- [2] Proch D 1999 *Handbook of Accelerator Physics and Engineering* ed A W Chao and M Tigner (Singapore: World Scientific) p 526
- [3] Proch D 1998 *Rep. Prog. Phys.* **61** 1
- [4] Padamsee H and Knobloch J 1996 *Frontiers of Accelerator Technology* ed S I Kurokawa *et al* (Singapore: World Scientific) p 101
- [5] Weingarten W 1996 *Frontiers of Accelerator Technology* ed S I Kurokawa *et al* (Singapore: World Scientific) p 311
- [6] Padamsee H *et al* 1993 *Ann. Rev. Nucl. Sci.* **B 43** 635
- [7] Padamsee H, Knobloch J and Hays T 1998 *RF Superconductivity for Accelerators* (New York: Wiley)
- [8] Reece C *et al* 1999 *Proc. 9th Workshop on RF Superconductivity* ed B Rusnak, paper MOA004
- [9] Brown P *et al* 1999 *Proc. 9th Workshop on RF Superconductivity* ed B Rusnak, paper MOA001
- [10] Belomestnykh S 1999 *Proc. 1999 Particle Accelerator Conf.* ed A Luccio *et al*, p 272
- [11] Tajima T 1999 *Proc. 1999 Particle Accelerator Conf.* ed A Luccio *et al*, p 440
- [12] Trines D 1999 *Proc. 9th Workshop on RF Superconductivity* ed B Rusnak, paper FRA 003
- [13] Storm D W 1999 *Proc. 6th Workshop on RF Superconductivity* ed R M Sundelin, p 216
- [14] Bartsch M *et al* 1990 *Proc. 1990 Linear Accelerator Conf. (Albuquerque, NM), Report LA-12004-C* Los Alamos National Laboratory, p 372
- [15] Delayen J and Shepard K W 1990 *Appl. Phys. Lett.* **57** 514
- [16] Aune B *et al* 2000 *DESY Report* DESY-31
- [17] Knobloch J 1999 *Proc. 1998 Appl. Supercond. Conf., IEEE Trans. Appl. Supercond.* **9** 1016
- [18] Klein U and Proch D 1979 *Proc. Conf. of Future Possibilities of Electron Accelerators (Charlottesville, VA)* ed J S McCarthy, p N1–17
- [19] Brinkmann A *et al* 1999 *Proc. 9th Workshop on RF Superconductivity* ed B Rusnak, paper TUA007
- [20] Koechlin B *et al* 1996 *Supercond. Sci. Technol.* **9** 453
- [21] Palmieri V 1999 *Proc. 1999 Particle Accelerator Conf.* ed A Luccio *et al*, p 541
- [22] Gonin I *et al* 1999 *Proc. 9th Workshop on RF Superconductivity* ed B Rusnak, paper THA002
- [23] Geng R 1999 *Proc. 9th Workshop on RF Superconductivity* ed B Rusnak, paper TUP021
- [24] Chiaveri E 1996 *Proc. 1996 European Particle Accelerator Conf. (Barcelona, Spain)* ed S Myers *et al* (Bristol: Institute of Physics) p 200
- [25] Orlandi G *et al* 1994 *Proc. 6th Workshop on RF Superconductivity* ed R M Sundelin (Newport News, VA: CEBAF) p 718
- [26] Benvenuti C *et al* 1999 *Physica C* **316** 153
- [27] Durand C *et al* 1995 *Proc. 1994 Applied Superconductivity Conf., IEEE Trans. Appl. Supercond.* **5** 1107
- [28] Muller G 1996 *Proc. 5th European Particle Accelerator Conf. (Barcelona, Spain)* ed S Myers *et al* (Bristol: Institute of Physics) p 2085
- [29] Hein M 1999 *High-Temperature-Superconductor Thin Films at Microwave Frequencies* (New York: Springer)
- [30] Mattis D C and Bardeen J 1958 *Phys. Rev.* **111** 412
- [31] Halbritter J 1970 *Z. Phys.* **238** 466
- [32] Bonin B 1996 *Proc. CERN Accelerator School* CERN 96-03, p 191
- [33] Weingarten W 1999 *Frontiers of Accelerator Technology* ed S I Kurokawa *et al* (Singapore: World Scientific) p 363
- [34] Darriulat P 1998 *Proc. 1998 European Particle Accelerator Conf. (Stockholm, Sweden)* ed S Myers *et al*, p 179
- [35] Benvenuti C 1999 *Proc. 9th Workshop on RF Superconductivity* ed B Rusnak, paper MOA002
- [36] Peiniger M 1988 *Proc. 3rd Workshop on RF Superconductivity* ed K W Shepard (Argonne, IL: Argonne National Laboratory) p 503
- [37] Hein M A 1995 *Proc. 7th Workshop on RF Superconductivity (Gif sur Yvette, France)* ed B Bonin, p 267
- [38] Valet C *et al* 1992 *Proc. 1992 European Particle Accelerator Conf. (Berlin, Germany)* ed E H Henke *et al*, p 1295
- [39] Bonin B *et al* 1991 *Proc. 5th Workshop on RF Superconductivity* ed D Proch (Hamburg: DESY) p 210
- [40] Weingarten W 2000 *Physica C* at press
- [41] Golosovsky M 1998 *Proc. 8th Workshop on RF Superconductivity* ed V Palmieri and A Lombardi, p 295
- [42] Hays T *et al* 1998 *Proc. 8th Workshop on RF Superconductivity* ed V Palmieri and A Lombardi, p 789, *Particle Accel.* **61**
- [43] Weingarten W 1992 *Proc. CERN Accelerator School* CERN 92-03 p 318
- [44] Padamsee H 1985 *IEEE Trans. Magn.* **21** 1007
- [45] Kneisel P 1988 *J. Less-Common Met.* **139** 179
- [46] Safa H *et al* 1995 *Proc. 7th Workshop on RF Superconductivity* ed B Bonin, p 649
- [47] Kako E *et al* 1998 *Proc. 8th Workshop on RF Superconductivity* ed V Palmieri and A Lombardi, p 491
- [48] Visentin B *et al* 1999 *Proc. 9th Workshop on RF Superconductivity* ed B Rusnak, paper TUP015
- [49] Knobloch J *et al* 1999 *Proc. 9th Workshop on RF Superconductivity* ed B Rusnak, paper TUA004
- [50] Kneisel P *et al* 1999 *Proc. 9th Workshop on RF Superconductivity* ed B Rusnak, paper WEP019
- [51] Lilje L 1999 *Proc. 9th Workshop on RF Superconductivity* ed B Rusnak, paper TUA001
- [52] Saito K *et al* 1999 *Proc. 9th Workshop on RF Superconductivity* ed B Rusnak, paper TUP003
- [53] Palmer F 1988 *PhD Thesis* Cornell University
- [54] Kneisel P *et al* 1999 *Proc. 9th Workshop on RF Superconductivity* ed B Rusnak, paper TUP031
- [55] Knobloch J 2000 Private communication, Cornell University
- [56] Graber J 1993 *PhD Thesis* Cornell University
- [57] Padamsee H 1999 *High Energy Density Microwaves (AIP Conf. Proc. Vol 474)* ed R M Phillips, p 212
- [58] Knobloch J *et al* 1998 *Particle Accel.* **61** 433
- [59] Knobloch J *et al* 1998 *Particle Accel.* **61** 169
- [60] Bernard Ph *et al* 1992 *Proc. 1992 European Particle Accelerator Conf.* ed E H Henke *et al*, p 1269
- [61] Saito K *et al* 1994 *Proc. 6th Workshop on RF Superconductivity* ed R M Sundelin, p 1151
- [62] Kneisel P *et al* 1994 *Proc. 6th Workshop on RF Superconductivity* ed R M Sundelin, p 628
- [63] Crawford C *et al* 1995 *Particle Accel.* **49** 1
- [64] Graber J *et al* 1994 *Nucl. Instrum. Methods* **350** 572